10/10/13/94 JSD

SANDIA REPORT

SAND93—1380 • UC—261
Unlimited Release
Printed June 1994

The Application of Non-Destructive Techniques to the Testing of a Wind Turbine Blade

Herbert Sutherland, Alan Beattie, Bruce Hansche, Walt Musial, Jack Allread, Jim Johnson, Mike Summers

Prepared by
Sandia National Laboratories
Albuquerque, New Mexico 87185 and Livermore, California 94550
for the United States Department of Energy
under Contract DE-AC04-94AL85000

Issued by Sandia National Laboratories, operated for the United States Department of Energy by Sandia Corporation.

Available to DOE and DOE contractors from
Office of Scientific and Technical Information
PO Box 62
Oak Ridge, TN 37831

Prices available from (615) 576-8401, FTS 626-8401

Available to the public from
National Technical Information Service
US Department of Commerce
5285 Port Royal Rd
Springfield, VA 22161

NTIS price codes
Printed copy: A04
Microfiche copy: A01

DISCLAIMER

Portions of this document may be illegible in electronic image products. Images are produced from the best available original document.

SAND93-1380
Unlimited Release
Printed June 1994

Distribution
Category UC-261

THE APPLICATION OF NON-DESTRUCTIVE TECHNIQUES TO THE TESTING OF A WIND TURBINE BLADE

Herbert Sutherland, Alan Beattie, and Bruce Hansche
Sandia National Laboratories; Albuquerque, NM 87185

Walt Musial, Jack Allread, and Jim Johnson
National Renewable Energy Laboratory; Golden, CO 80401

Mike Summers
United Technologies (Pratt & Whitney); West Palm Beach, FL 33410

ABSTRACT

NonDestructive Testing (NDT), also called NonDestructive Evaluation (NDE), is commonly used to monitor structures before, during, and after testing. This paper reports on the use of two NDT techniques to monitor the behavior of a typical wind turbine blade during a quasi-static test-to-failure. The two NDT techniques used were acoustic emission and coherent optical. The former monitors the acoustic energy produced by the blade as it is loaded. The latter uses electronic shearography to measure the differences in surface displacements between two load states. Typical results are presented to demonstrate the ability of these two techniques to locate and monitor both high damage regions and flaws in the blade structure. Furthermore, this experiment highlights the limitations in the techniques that must be addressed before one or both can be transferred, with a high probability of success, to the inspection and monitoring of turbine blades during the manufacturing process and under normal operating conditions.

CONTENTS

CONTENTS (Continued)

Figures

Figures (Continued)

1. INTRODUCTION

NonDestructive Testing (NDT) is a powerful tool for reducing costs, improving and maintaining product quality, and inspecting in-service components. The use of NDT techniques, also called NonDestructive Evaluation (NDE), is common in a number of industries, especially the aircraft industry, for quality control (QC) and quality assurance (QA). However, the use of NDT for the inspection and testing of wind turbine has not been used widely. One notable exception is the QA program adopted by Gougeon Brothers [1]. They have used acoustic waves to inspect and control the quality of the wood veneer used in the construction of their wind turbine blades. The primary reason that NDT techniques have limited use in the wind turbine industry is that suitable test systems and procedures for the inspection of wind turbine components have not been demonstrated to be cost-effective and reliable.

To demonstrate the use, reliability, and abilities of typical NDT techniques, Sandia National Laboratories (SNL) and the National Renewable Energy Laboratory (NREL) have initiated a program under the auspices of the DOE Wind Energy Technology Program. The initial phase of this "proof-of-concept" program is concentrating on NDT techniques that have a high potential for use as QA tools in the manufacturing of wind turbine blades and for in-service inspection of blades. This paper discusses the use of two NDT systems: acoustic emission [2] and coherent optical [3]. To facilitate the testing of these techniques on a typical wind turbine blade, a quasi-static test-to-failure of a full blade was conducted in the NREL full-blade test fixture [4]. The blade chosen for this experiment is the Phoenix-built, thin-airfoil 7.9 m blade [5, 6]. It was loaded to failure in Phase 1 of the experiment using hydraulic rams at three points with a load distribution that simulated the load distribution on the blade under field operation. In Phase 2, the unbroken portion of the blade was loaded to failure using a single point load.

The acoustic emission system used here employs 12 sensors located at various stations on the blade, and another 12 sensors concentrated around the root section of the blade. Data from the sensors were recorded and then processed after the experiment was completed. Some real-time information was available from the system during the experiment. The data processing used here determines the location(s) of structural damage using both time and amplitude techniques. The "signature" of the acoustic emissions also permits the class(es) of failure mechanisms developed in the structure to be ascertained.

The coherent optical technique used electronic speckle pattern shearography. The system used here is a commercial system provided by United Technologies (Pratt & Whitney) and it

measures differences in surface displacements between two load states with an accuracy of a few microns. Two loading systems were used. For pre- and post-test inspection, the blade was loaded thermally. The typical structural loads were used during the course of the experiment. The system was able to locate "flaws" and internal structure in the blade. For the pre-test inspection, the entire blade surface was inspected. The location of flaws and internal structure were marked on the blade. An area, approximately 2-feet on each side, near the root of the blade, was monitored during the course of the test. The post-test inspection examined previously identified flaws and the failed portions of the blades. This technique was able to identify flaws and their growth during the course of the experiment.

This paper presents the details of this proof-of-concept experiment and discusses the applicability of the acoustic emission and coherent optical NDT techniques to the inspection of wind turbine blades.

2. THE QUASI-STATIC BLADE TEST

The quasi-static blade test was conducted on a 7.9-m blade in the NREL full-blade test facility [4]. The blade was loaded to failure in a two-phase test program. In the first phase, a distributed load that simulates field loads was used to load the blade to failure. The first phase produced a failure of the blade near its tip. In the second phase, the remaining section of the blade was loaded to failure with a single point load. This failure produced a failure of the blade's spar and skin structure near the root section of the blade.

2.1 Blade Test Specimen

The quasi-static blade test was conducted on an NREL 7.9 m blade; see Figure 1. The blade geometry was designed using the NREL thin airfoil family [5]. It was fabricated at Phoenix Industries in Crookston, MN for NREL to demonstrate the performance of the NREL airfoils. Although the blade root was designed to be interchangeable with a standard Aerostar 7.5 m blade used on many of the operating wind turbines in California wind turbine power plants, the test blade root differs from the original Aerostar design. The test blade root used a flanged steel insert rather than the Aerostar blade's Hutter root configuration. The test blade, along with two other blades of this design, operated for 10,000 hr on a Micon 65 wind turbine in San Gorgonio Pass in California prior to this test. The blade was constructed primarily of fiberglass reinforced polyester with a total weight of 633 lb.

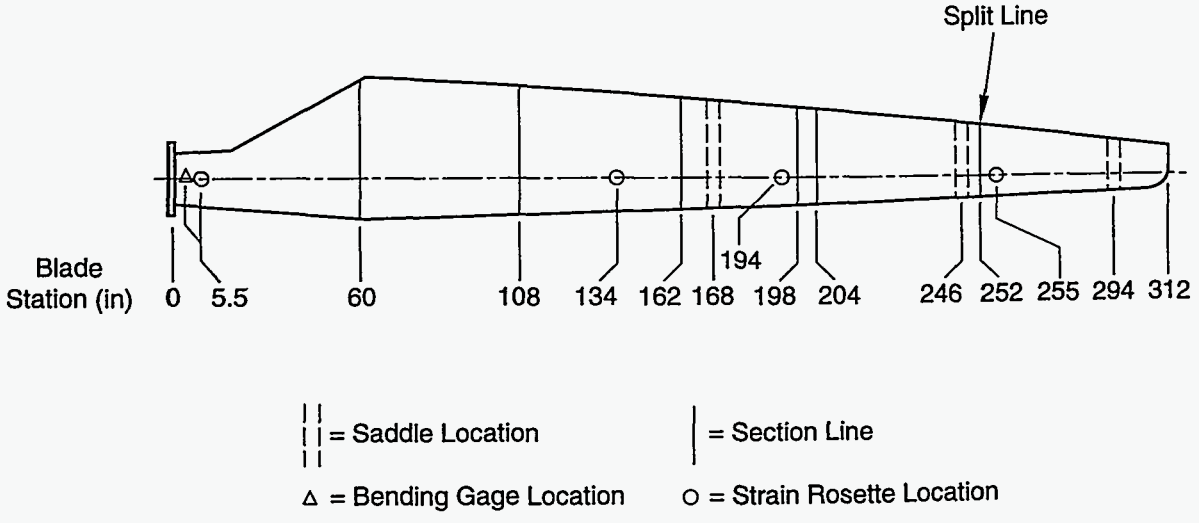

Figure 1. Schematic diagram of the NREL 7.9 meter blade.

2.2 Blade Loads

2.2.1 Phase 1

For Phase 1 of the experiment, the blade was loaded using a three-point spanwise load distribution. This load distribution is a good approximation to the loads imposed on the blade during its operation.

2.2.1.1 Typical Field Loads. Operating loads were measured on the root of Micon 65/13 wind turbine in San Gorgonio Pass in California [6]. The turbine was fitted with the NREL 7.9 m blade. A total of 67.5 hours of data was taken in 405 ten-minute records. Figures 2 and 3 show the maximum and minimum peak flap bending moments for the entire data set as a function of the number of occurrences. As seen in these two figures, the maximum mean blade bending moment is approximately 54 ft-kips (40 kNm). These data characterize the root bending loads for this blade but do not define the load distribution along the blade span that is required to conduct a static test of the blade with realistic loads.

2.2.1.2 Experimental Loads. In July 1989, quasi-static tests were conducted on the Phoenix 7.9 m blade by Phoenix Industries at North Dakota State University (NDS) [4]. In these tests, the blade was loaded in the flapwise direction using sandbags placed at ten evenly spaced blade stations. This loading produced a triangular load distribution; see Figure 4. The centroid of load distribution was located at approximately Station 100. This loading is used commonly to represent the load distribution on a wind turbine blade.

The loading used in the first phase of this experiment uses a three point load to approximate the triangular load used at NDS; see Figure 4. This figure shows that the three point load distribution is a good approximation of the ten point triangular distribution. The three point loads on the blade are at stations 168, 246 and 294. The load ratio at these stations are 42.5, 39.2 and 18.3 percent, respectively. This load distribution was achieved using a single point load attached to the blade with a series of spanner beams and compliant links, called a whiffle tree; see Figure 5. The load was applied to the whiffle tree using a gantry crane, equipped with a hydraulic winch. A load cell was placed between the two to monitor the total applied load on the blade. The distributed three-point loads were applied to the blade via saddles constructed from laminated plywood. The plywood was cut to fit the blade's airfoil profile and padded with

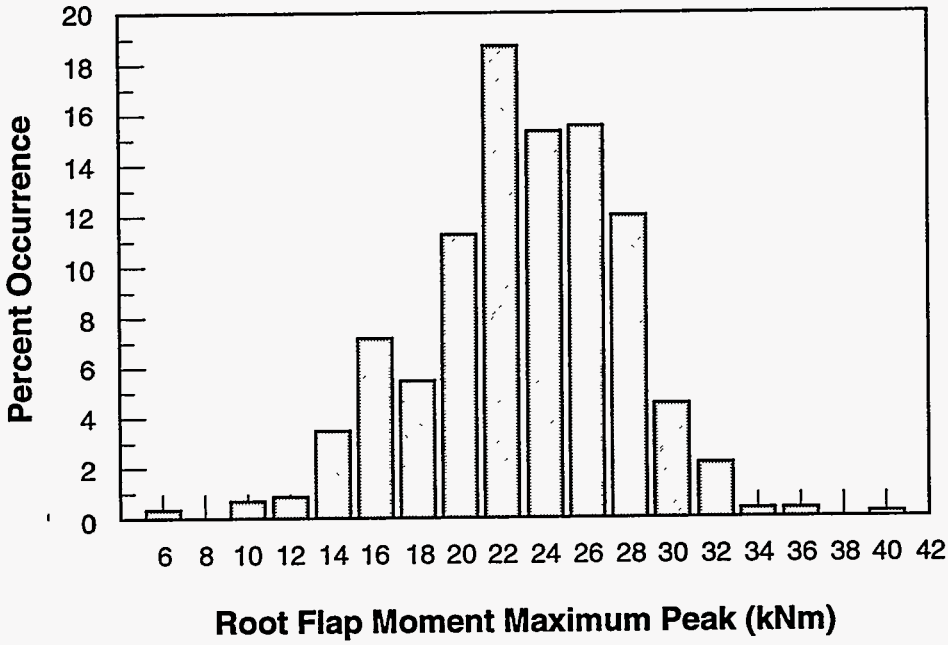

Figure 2. Root flap bending moments, measured maximum peaks.

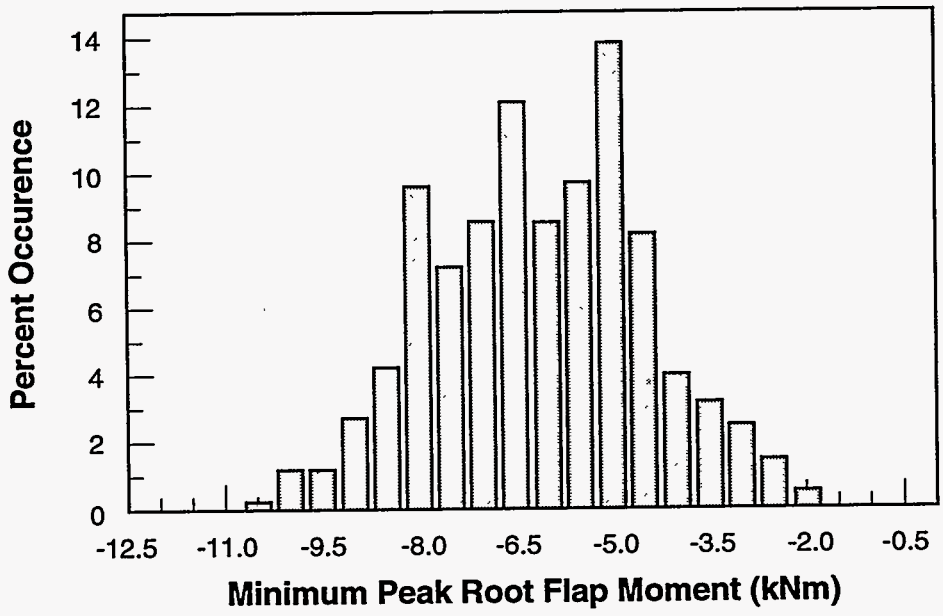

Figure 3. Root flap bending moments, measured minimum peaks.

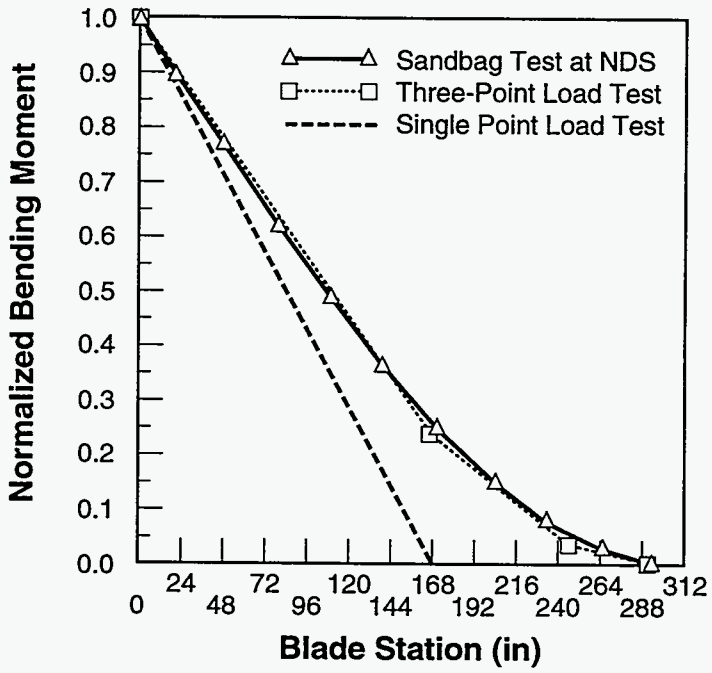

Figure 4. Bending moment distributions.

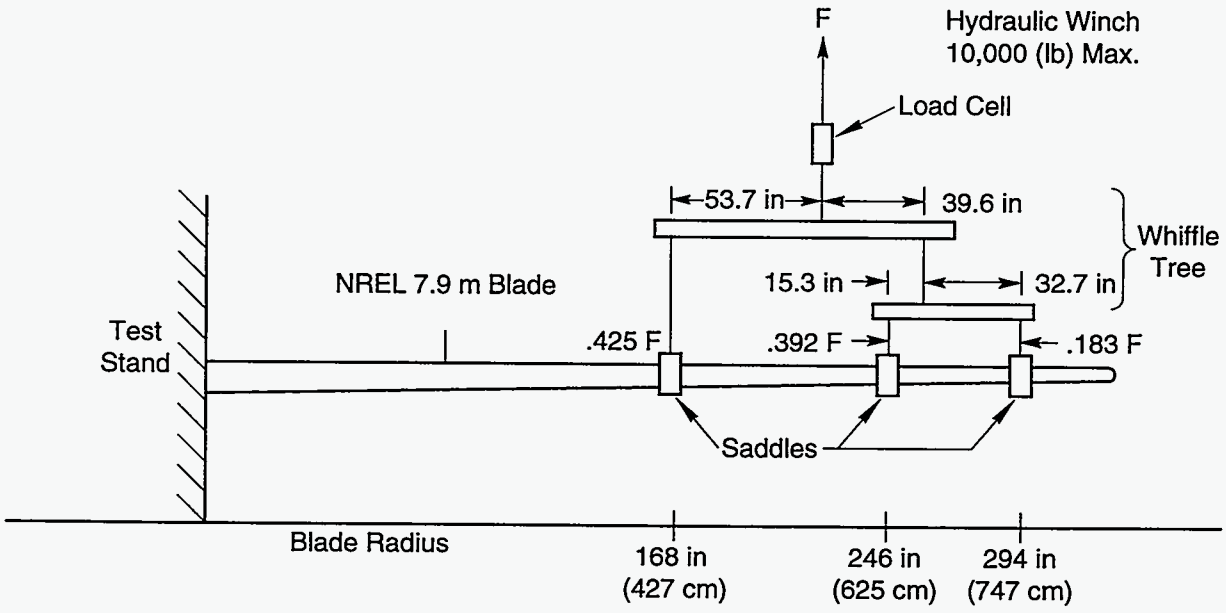

Figure 5. Whiffle tree geometry.

neoprene. The neoprene served to evenly distribute the load across the width of the saddle, i.e., a width of approximately 6 in. (152 cm).

There were several constraints that guided the selection of the load distribution for this phase of the test. The number of load points was limited to three to minimize potential interruptions of acoustic transmission along the blade span. The load distribution was tailored to diminish the bending moment at the split line of the pitching tip. This choice avoids failure of the tip at the split line. Also, the saddle locations were selected to avoid reinforcing potential stress concentrations, such as the area enclosing the pitch mechanism.

Loads were applied at the 25 percent chord stations, except at the tip where load application point was at 40 percent chord, corresponding to the location of the pitch shaft of the tip mechanism. Saddles were designed to account for the blade twist as the blade is loaded in the flapwise direction.

2.2.2 Phase 2

Since the majority of the blade's structure was still intact after the first failure, the blade test was continued with a second phase of loading. This phase used a single point load at blade station 168. For both of these tests, the load cell was connected directly to the saddle attachment (at station 168) and the whiffle tree was removed.

2.3 Instrumentation

The primary monitor used in this experiment was a series of strain gauges located along the span of the blade. Most of the strain gauges were three element rectangular rosettes with 1000 ohm elements. These gauges were placed at four spanwise locations on the high pressure (tension) side of the blade. The span-wise strain gauges were at stations 5.5, 134, 194 and 255, respectively. Also, a half bridge bending gauge was located at station 5.5. The locations of the strain gauges are shown in Figure 1.

Strain gauge locations were determined from measurements made in a previous test of a Phoenix 7.9 meter blade in which photoelastic techniques were employed to locate areas of high

strain in this blade [4], and from earlier static testing. The bending gauge at station 5.5 was used as a reference for the blade loads. Station 134 was selected for monitoring because the blade tested at NDS failed at this location. Stations 194 and 255 were located near the pitch mechanism. These areas appeared as relatively high stress areas in the photoelastic tests.*

Fourteen channels of data were taken during the blade test. Twelve channels monitored the strain measurements from the rectangular rosettes, one channel monitored the blade bending strains, and the final channel monitored the load cell force. All signals received bridge completion, bridge excitation, low-pass filtration at 10 Hz, and signal amplification from Honeywell 218 bridge amplifiers. A Keithly Model 500 analog-to-digital interface was used to convert the analogue output of the Honeywell amplifiers into a digital format for a DOS based data-acquisition computer.

The blade deflections were measured at each of the three saddle locations. This measurement used pointers that were attached to the blade. Displacements were measured manually using the floor as a reference plane.

The acoustic emission and coherent optical instrumentation are described in detail below.

2.4 Test Procedure

Several steps were taken to prepare the blade for testing. The first step insured that the strain measurements were referenced to an unloaded blade condition. To achieve this state, the blade was supported in a zero bending position prior to its installation on the blade stand, and the strain gauge outputs were zeroed. After the blade was mounted, the strain gauges were calibrated by pulling up on the blade at a single location. The loading apparatus, including saddles, whiffle tree beams and links and fasteners, was weighed prior to installation on the blade. The loading apparatus was then assembled and installed on the blade. Deflection scales and pointers were placed at each of the saddle locations along the blade. A video camera was set up to document

---

* The blade tested here and the blade tested with photoelastic strain measurements were not identical. The two blades had different pitch mechanisms, which could alter the stress patterns in this region of the blade. However, our experience indicated that this area of the blade is still relatively highly stressed.

the test. Simultaneously, acoustic sensors and laser shearography equipment were set up along the blade. The data acquisition program was started just prior to blade loading.

The blade loading was divided into two main phases. Phase 1 of the test used the three-point load whiffle tree described in Figure 4. This loading was used until the initial blade failure occurred. Since the majority of the blade's structure was still intact after the first failure, Phase 2 blade tests were conducted using just the saddle at 168 in. (427 cm) to load the blade. Each of these tests is described below.

2.4.1 Phase 1

During phase 1 testing, the initial load on the blade was 1000 lb (4.5 kN). Strain gauge data were recorded continuously at a 20 Hz sampling rate. Deflection measurements were taken manually at each 1000 lb (4.5 kN) load interval. When 2000 lb (8.9 kN) was reached, the load intervals were reduced to 500 lb (2.2 kN) increments until failure occurred. Figure 6a shows the load vs time plot for this set of loads. After failure at 3925 lb (17.5 kN), the blade was unloaded and the failure locations were documented. A photograph of the blade under three-point loading is shown in Figure 7.

2.4.2 Phase 2

Phase 2 of the test used just the saddle at station 168 to load the blade. The load cell was connected directly to the saddle attachment, and the whiffle tree was removed. The load distribution for this loading is shown for comparison in Figure 4. After each of the two blade failures, the blade was unloaded and the failure locations were documented.

2.4.2.1 Phase 2a. For this phase of the testing program, the blade was loaded at station 168 to approximately 6400 lb (28.5 kN), where first failure of the blade occurred. This loading sequence is shown in Figure 6b.

2.4.2.2 Phase 2b. For this phase of the testing program, the blade was loaded at station 168 to approximately 9000 lb (40.0 kN). This loading sequence is shown in Figure 6c.

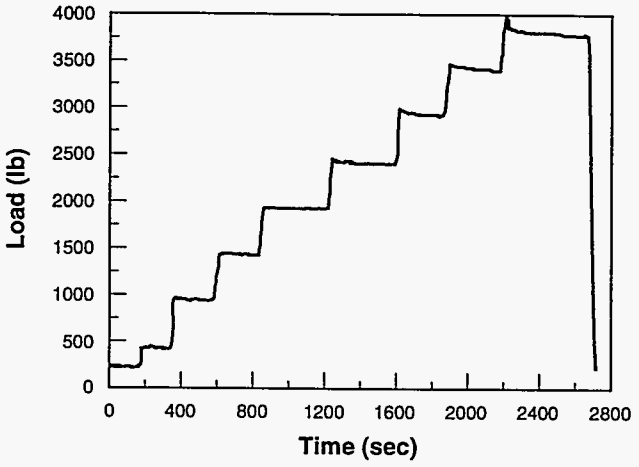

Figure 6a. Phase 1 loading.

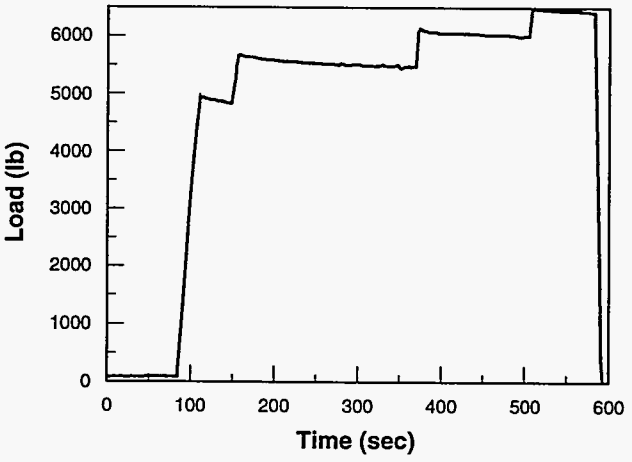

Figure 6b. Phase 2a loading.

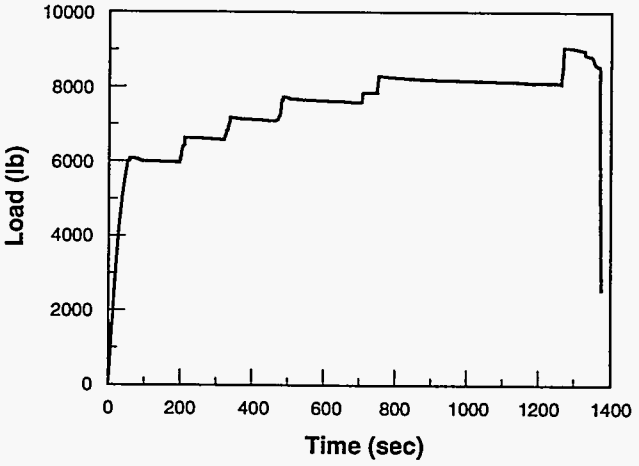

Figure 6c. Phase 2b loading.

Figure 6. Load histories.

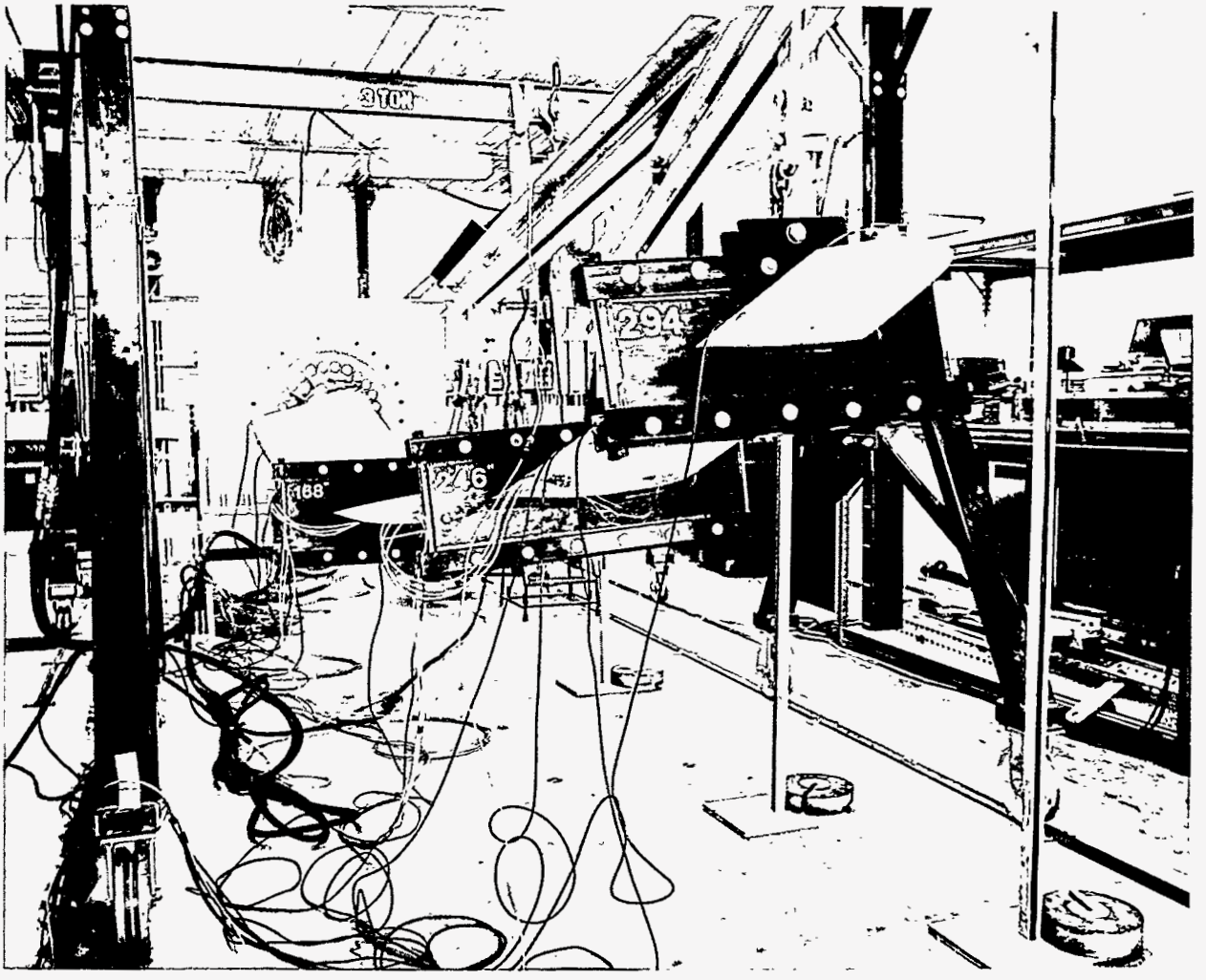

Figure 7. Phase 1 blade test.

2.5 Test Results

2.5.1 Phase 1

The Phase 1 test resulted in a failure of the blade at approximately station 240. This station is located approximately 12 in. (30.5 cm) inboard from the split line of the pitchable tip at station and approximately 6 in. (15.2 cm) inboard from the middle saddle used to load the blade. The failure occurred near the point where the internal spar (shear web) was terminated and the pitch shaft transitions to a smaller diameter shaft. The peak load recorded at failure was 3925 lb (17.5 kN) on the load cell; see Figure 6a. This load results in a root failure load of 72,528 ft-lb (97.9 kN-m). The bending moment at the failure location due to the force on the outer two saddles was 3596 ft-lb (4.8 kN-m). The failure appeared as a cordwise crease in the skin on compression surface.

2.5.2 Phase 2

Phase 2 loading of the blade used a single point load. The blade failed first, Phase 2a loading, at approximately 6400 lb (28.5 kN). This failure was primarily a crushing of the blade skin and/or the shear web beneath the saddle used to load the blade.

Phase 2b loading resulted in a failure of the blade structure over a large spanwise section extending from station 100 to the saddle at station 164. The failure was a complete debonding of the trailing and leading edge and a buckling of the internal shear web and blade skin. The peak load reached under this test was 8996 lb (40.0 kN) which resulted in a peak root bending moment of 125,944 ft-lb (170 kN-m). Although the applied root load was significantly higher during the Phase 2 loading, the bending moments calculated at station 134, in the middle of the section that failed under Phase 2b loading, were smaller than the bending loads during the Phase 1 loading.

At failure the bending moments at station 134 were 28,663 ft-lb (38.9 kN-m) during the three point load test and were 25,489 ft-lb (34.6 kN-m) during the second load test.

2.5.3 Strain Measurements

Blade strains were monitored during the course of the test at each of the strain gauge locations. Blade strains are shown versus blade load for key gauge locations along the blade in Figures 8 through 13. Figures 8 through 11 show the longitudinal and transverse strains for each of the four gauge locations during the Phase 1 loading sequence. Note that the highest strains occurred at stations 134 and 194, Figures 9 and 10, respectively. Strains at these locations were over an order of magnitude higher that the root strains. Strains at station 255 were in the same range as the root strains. Figures 12 and 13 show the strains for the two inboard gauges during Phase 2b. The other gauges were not plotted because they were outboard of the pull point.

2.5.4 Blade Deflections

Blade deflections were measured at the three saddle locations along the blade during the Phase 1 loading. Vertical scales were placed adjacent to the saddles. Horizontal pointers were attached to the saddles, which moved upward with the blade as the load was increased. Measurements were taken manually at each load increment, using a surveyor's transit to read the scales. The blade deflections are shown for each saddle location versus load in Figure 14. The three deflection curves show that some tip damage was beginning to occur at the last load interval, as evidenced by the nonlinear bend in the curve.

2.6 Post-Test Inspection

The failed blade was sectioned as shown in Figure 1. The areas of interest isolated for a closer inspection of the failure regions were the primary failure (Phase 1 loading) at station 240, the region of the tip mechanism, and the secondary failure (Phase 2) at approximately station 150. Other areas of interest, identified by the laser shearography and/or the acoustic emissions, were also examined. These major areas were sectioned, and detailed inspections conducted.

Visual examination of the primary (Phase 1) failure at station 240 showed that the steel pitch shaft of the tip spoiler mechanism (see Figure 15) was bent inboard of the cam mechanism. The skin was also buckled on the low pressure side of the blade in the same radial location as the failure of the steel tip mechanism itself; see Figure 16. This failure location also coincides with the termination of the internal shear webs; see Figure 15.

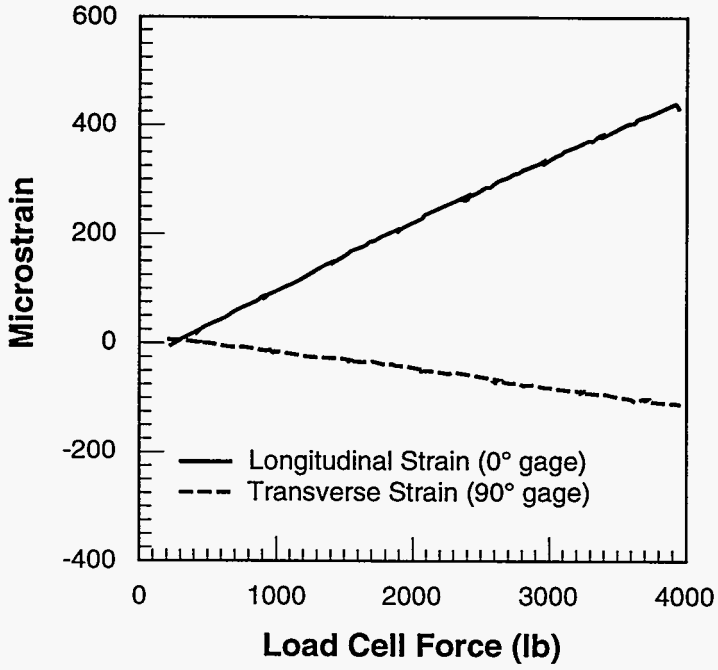

Figure 8. Blade root strains for Phase 1 loading.

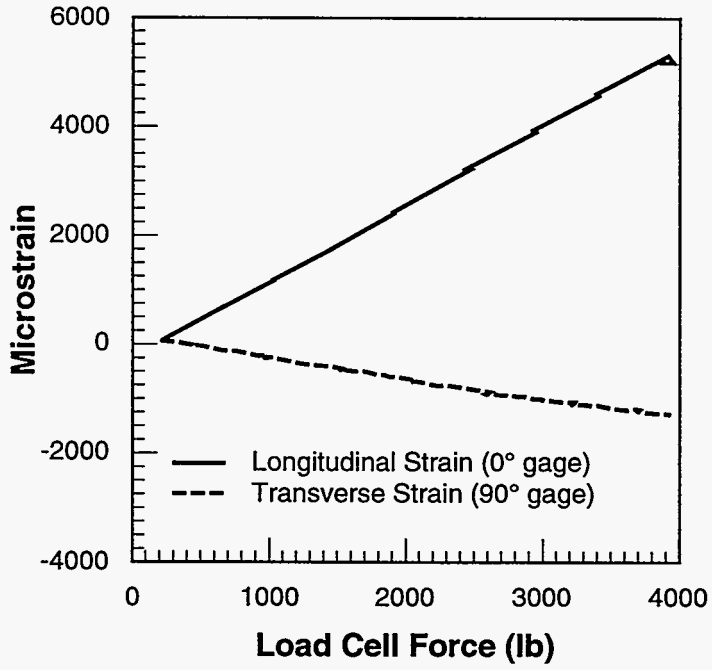

Figure 9. Blade skin strains at station 134 for Phase 1 loading.

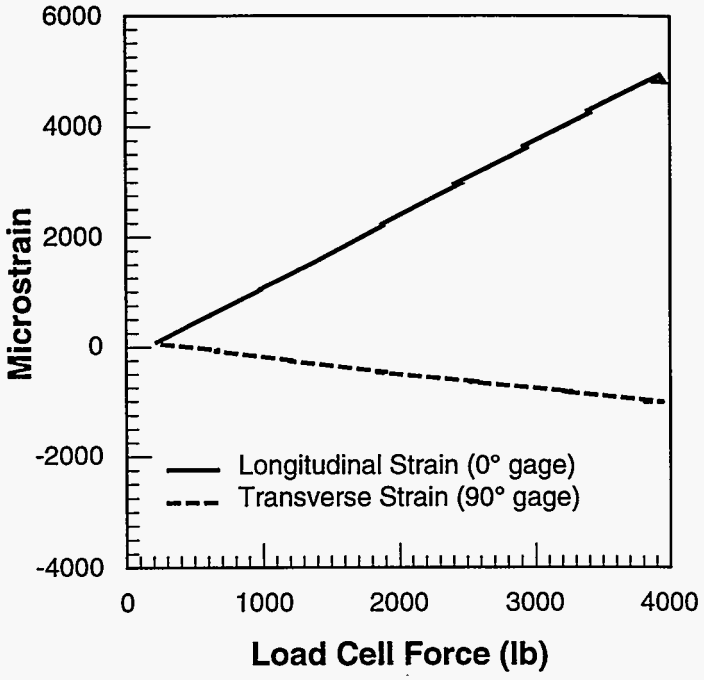

Figure 10. Blade skin strains at station 194 for Phase 1 loading.

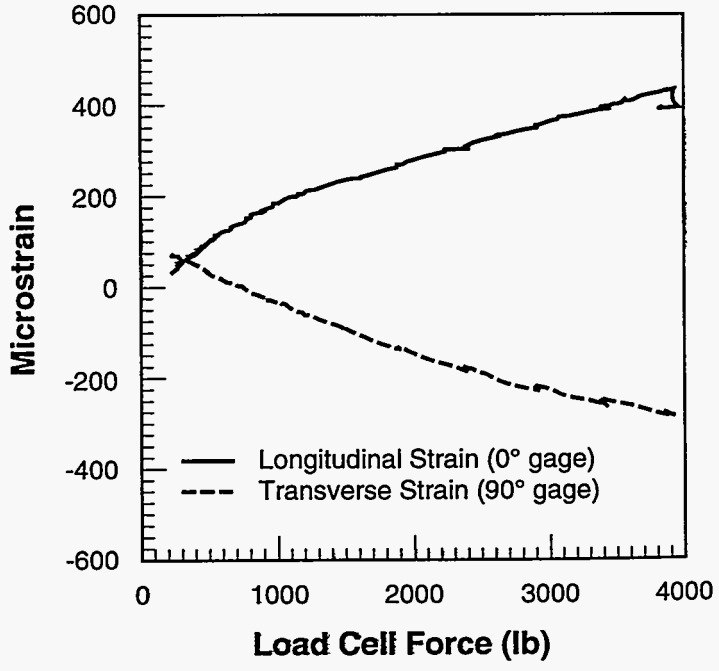

Figure 11. Blade skin strains at station 255 for Phase 1 loading.

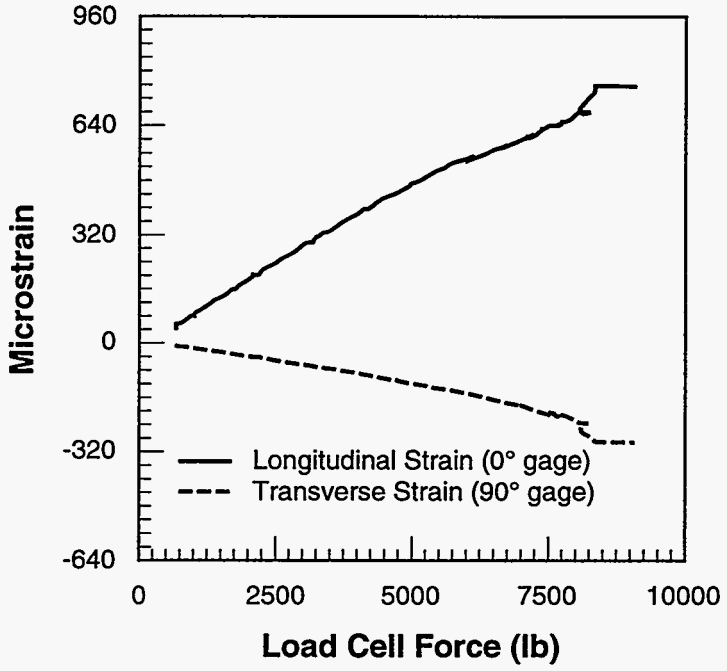

Figure 12. Blade root strains for Phase 2 loading.

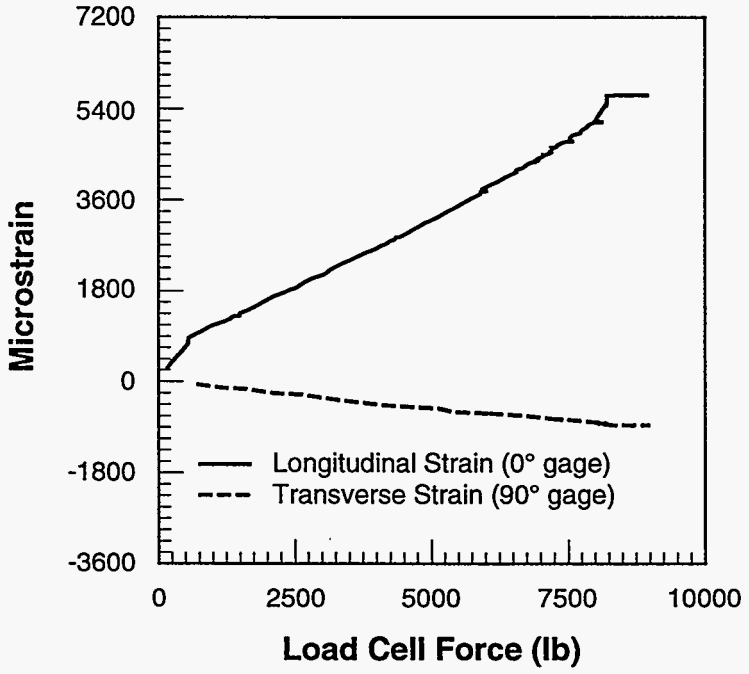

Figure 13. Blade skin strains at station 134 for Phase 2 loading.

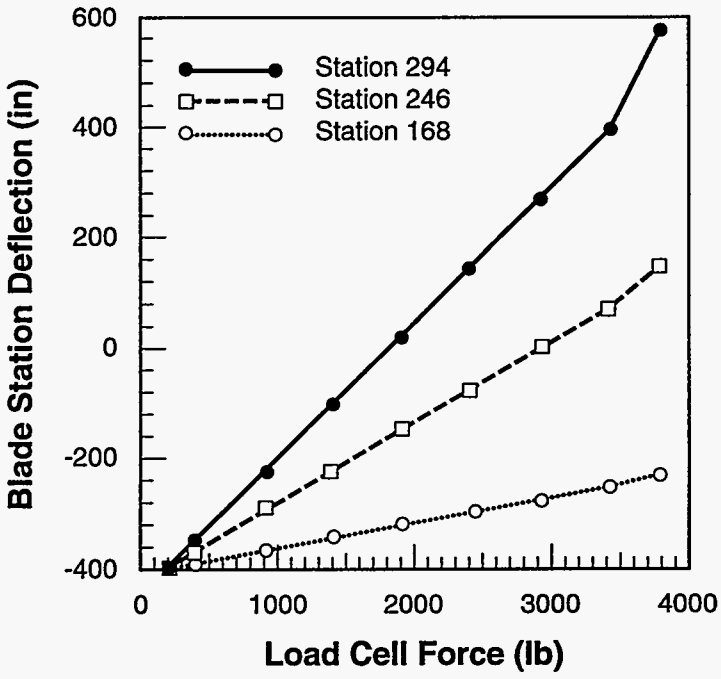

Figure 14. Blade deflections for Phase 1 loading.

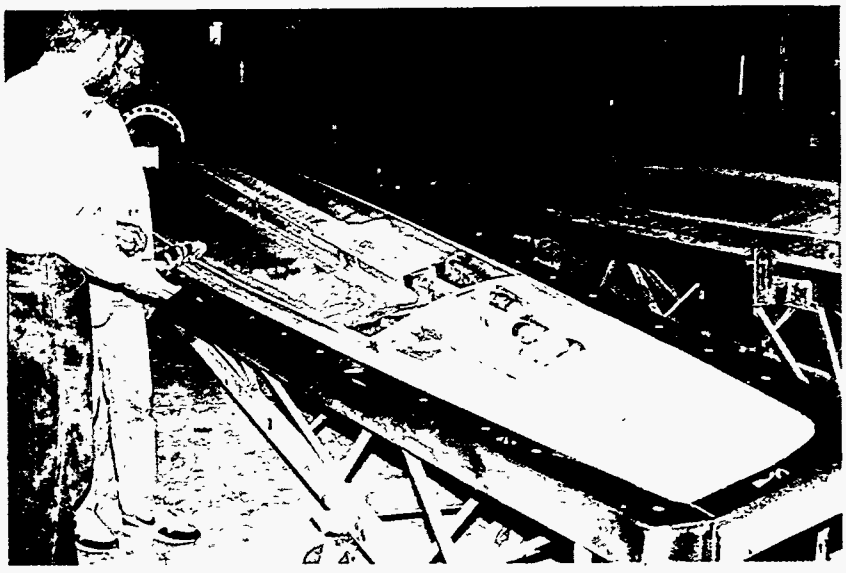

Figure 15. Internal structure of the NREL 7.9 meter blade.

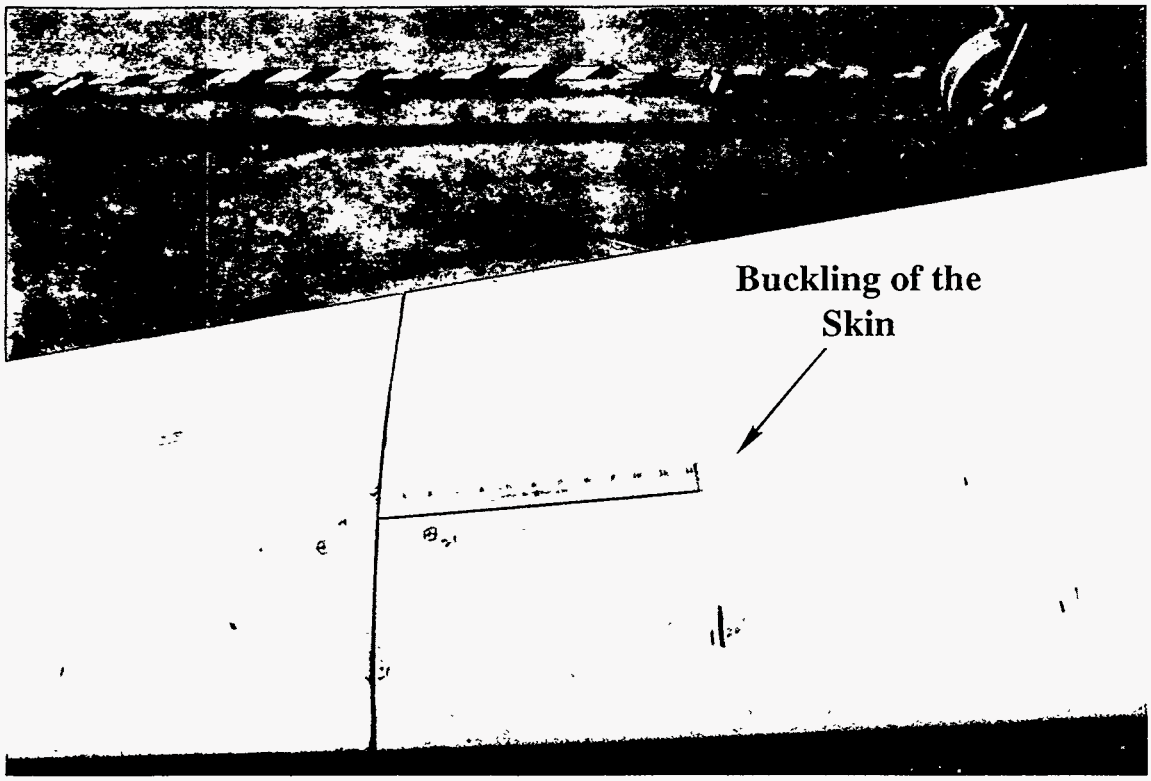

Figure 16. Blade failure for Phase 1 loading, buckled skin at station 240.

The secondary (Phase 2a and 2b loading) failure occurred between stations 100 and 168 due to the single-point load applied at station 168. Visual examination showed that the shear webs failed in compression in this area. The station 168 saddle used to apply the single-point load crushed the skin on the high pressure side of the blade. These locally high stresses may have been the initiation point for some of the delaminations that propagated from the leading and trailing edges during the secondary failure.

Descriptions of these failed areas and the other areas of interest are described in detail in Section 3.

3. THE ACOUSTIC EMISSION TECHNIQUE

3.1 Acoustic Emissions

Acoustic emissions (AE) are acoustic waves generated by a material when it undergoes inelastic strain or rupture [2]. In the case of fiberglass, there are three main sources of emission. These are a) matrix cracking, b) fiber fracture and c) fracture of the fiber-matrix interface. A tear in the fiberglass will involve all three mechanisms. Which of the mechanisms will generate emission at a point in a test will depend upon the material characteristics and the locally applied stress field in every region in the material. The presence of acoustic emission in a fiberglass structure subjected to an external load indicates a local failure in some part of the structure. During the initial loading or at loads low compared to the design load, fiberglass often generates some acoustic emission. Emission under these circumstances often does not signify significant flaws but is produced in localized regions of high residual stress such as an overtight wrap in a wrapped fiberglass vessel.

In a large fiberglass structure, the optimum use of acoustic emission testing involves spatial location of the acoustic emission sources. One common way of locating acoustic emission is by covering the surface of the vessel with sensors spaced in such a way that a single emission will excite only one or two sensors. This is often possible because of the relatively large frequency-dependent acoustic attenuation of fiberglass. Such a method is adequate for a proof test to determine the safety of a vessel, but is of little use in a research project. Another method of source location is to determine the arrival time of an individual emission burst at different sensors. Two sensors must be activated by the emission for linear location, and three or more must be activated for two dimensional location. Three dimensional location is possible in simple structures or samples but it is essentially impossible for a structure as complex as a fiberglass wind turbine blade. The main problem with source location in fiberglass is the very high acoustic attenuation. At moderate acoustic emission frequencies, a two dimensional source location setup covering the entire surface of a wind turbine blade could require a prohibitive number of sensors.

3.2 Experimental Design and Setup

3.2.1 AE Signal Attenuation

The key parameter in setting up an AE location test on a fiberglass structure is the acoustic attenuation. To measure the attenuation, a small section of a wind turbine blade with a construction similar to the test blade was obtained. After experimenting with several sensor bonding materials, a silicone bath tub caulk (MD Silicone bathroom sealant) was selected. This material gave good adhesion and good acoustic coupling. The caulk is flexible enough to absorb some differential strain between the fiberglass and the sensor. An acoustic sensor was then bonded to the test section, and the pencil lead break technique was used to introduce signals at different distances [2]. The detected signals were digitized and stored. FFTs were calculated and the total signal energies in each 25 kHz band between 0 and 250 kHz were determined. The attenuation coefficient for each band was determined by using a linear fit to the signal energy vs distance plot for each frequency band. The results for this sample are plotted in Figure 17.

The blade section used here was constructed using foam to reinforce the trailing edge of the blade. As determined in preliminary tests on a section of the blade, the regions of the blade that contained the foam absorbed much of the acoustic energy above 20 kHz.

To determine the location of an AE event requires "time of flight" measurements. For this measurement to be accurate, the signals arriving at different sensors should have approximately the same amplitudes. However, signals with differences of as much as 30 dB will still allow their location to be determined (if they are detected), although with reduced accuracy. At a center frequency of 150 kHz (a typical center frequency for AE transducers), a maximum spacing of 9.9 in. (25 cm) is required to meet this 30 dB criteria. As the AE system used here has 24 channels, this comparatively close spacing would have limited the AE portion of this test to selected parts of the blade. However, by changing to transducers with a 60 kHz center frequency, the AE coverage could be extended to the whole blade. Using the 60 kHz transducers, the 30 dB criteria permit a spacing of 32 in. (81 cm). Figure 18 shows the spectral response of the 60 kHz sensors. As shown in this figure, they have a reasonable response down to 40 kHz. Thus, these transducers permit a fairly accurate determination of the location of AE events on the test blade.

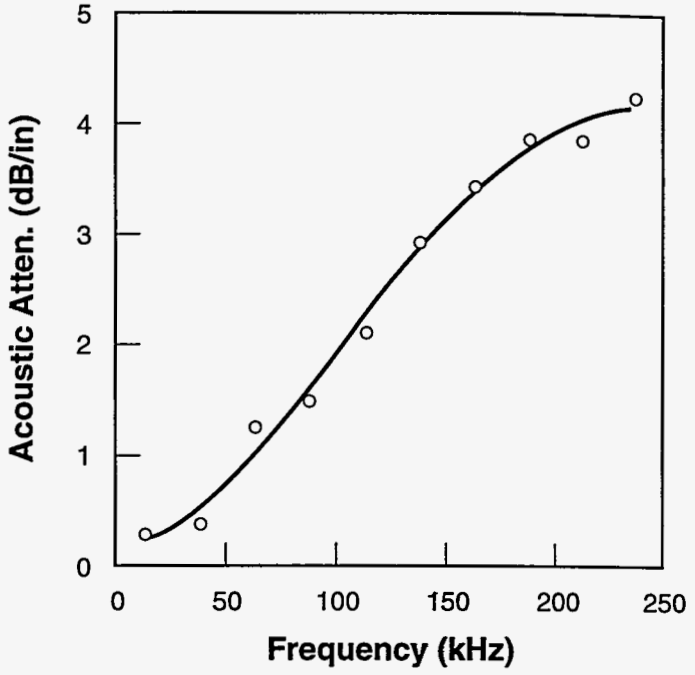

Figure 17. Acoustic attenuation in a fiberglass wind blade material.

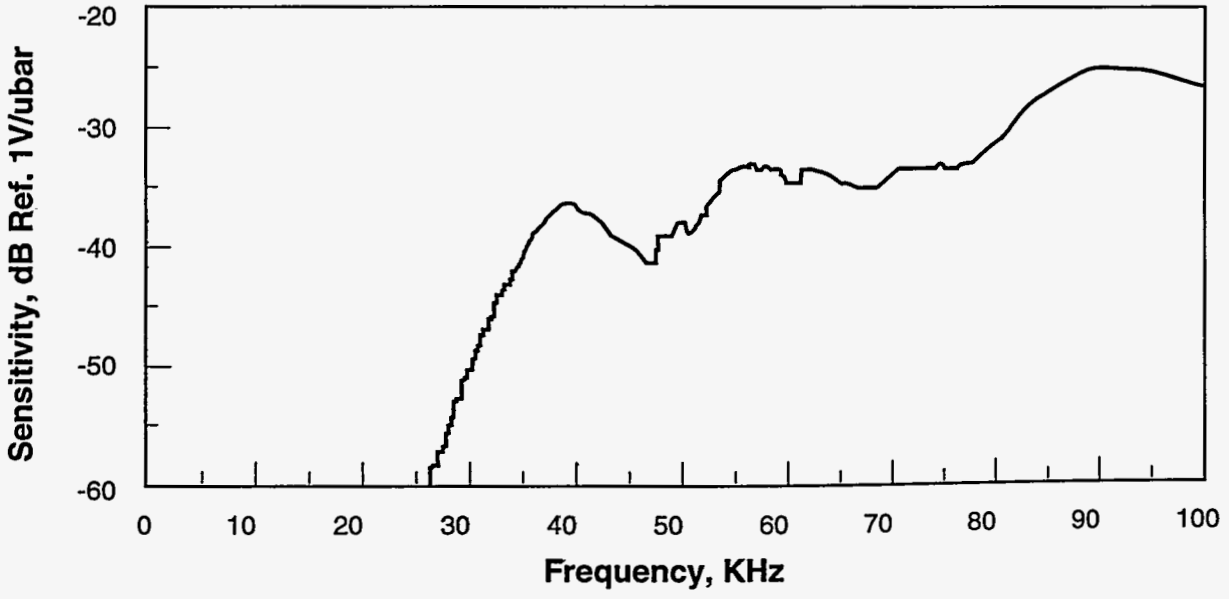

Figure 18. Spectral response of the 60 kHz AE sensors.

3.2.2 Locating AE Events

To perform accurate source location, the acoustic velocity in the material must be known. As this information was not known *a priori* for the materials in the test blade, the acoustic velocity in the blade had to be measured. Here, we used a time-of-flight measurement to determine the acoustic wave velocity [2]. In this technique, an acoustic signal is created by breaking a pencil point on the surface of the blade. The signal generated is then recorded by two sensors. One sensor is mounted relatively close to the signal source and the other is mounted approximately 19.5 in. (50 cm) away. To achieve the best accuracy in this measurement, the "first arrival" of the acoustic wave is used to determine the velocity. Unfortunately, the attenuation and dispersion in the fiberglass precluded the use of this measurement. Another technique for the determination of the acoustic velocity uses the time of flight of the first large peak in the signal. Using this technique, which is inherently less accurate than the first-arrival technique, the measured velocity in the fiberglass was 118,000 in/sec (3.0 mm/μsec).

This acoustic emission system triggers when the signal amplitude exceeds a preset value. If the attenuation is low or the source of the emission is close to the sensor, the system will trigger on the first cycle of the signal. In materials with high attenuation and high dispersion, such as fiberglass, the signal rapidly grows weaker as it travels from its origin and the point of maximum amplitude in the signal moves toward the rear of the signal (reference 2 contains a discussion of acoustic propagation and of signal detection). The result is that a signal which travels moderate distances in fiberglass may lose most of the acoustic energy in its initial cycles. Measurements on this blade showed that the apparent arrival time for a signal of moderate amplitude that travels 30 in. (75 cm) could have an apparent arrival time at the sensor of more than 100 microseconds later than the time without the effects of attenuation and dispersion. Such timing discrepancies can greatly affect the calculated location of the source.

The location algorithms used in this system calculate the location of a source between the first two detecting sensors for linear location or inside the triangle defined by the first three detecting sensors for planar location. To insure that the longer apparent acoustic flight times produced by attenuation and dispersion did not prevent the acceptance of signals from real events, a slower acoustic velocity was used in the algorithms. A value of 83,000 in/sec (2.10 mm/μsec) was used instead of 118,000 in/sec (3.00 mm/μsec). This ensured that all locatable signals were included in the analysis. The effect on the calculated locations is to move them closer to the midpoint between the two sensors or toward the middle of the triangle for the three

sensors. When one is trying to find the general region of failure, this minor shifting is of little significance compared to the possibility of throwing out large numbers of real events.

3.2.3 The AE System

A 24 channel PAC Spartan-AT system was chosen for this experiment because it has the ability to use sensors with integral preamplifiers. The sensors used here, PAC R6I, have 40 dB preamplifiers built into them. The gain on the PAC Spartan-AT system was set to amplify the signals another 20 dB.

The detection threshold for an AE event was set at a moderate level of 50 dB above 1 microvolt (316 mv). This sensitivity level was chosen to ignore low level noise. With this value, there is a possibility that some signals arising from matrix crazing would be ignored as well.

3.2.4 Transducer Location

The possibility of cracking in the root region of the blade suggested a detailed examination of the blade's root. Twelve transducers, numbered 1 through 12, were allocated for this section of the blade. The locations of these transducers are shown schematically in Figure 19a. In this figure, the circumferential distance around the root has been "unfolded" into a linear plot. The break line for this plot is at circumferential station 0 which is coincident with approximately circumferential station 60. Transducers 1 and 9 are on the compression side (top) of the blade, and transducers 3 and 11 are on the tension side (bottom) of the blade. The other twelve transducer, numbered 13 through 24, were located along the length of the top of the blade; see Figure 19b. The maximum spacing between any two sensors along the blade was 29.0 in. (73.7 cm), while the maximum spacing about the root was 14.5 in. (36.8 cm).

Before the start of the test, it was determined that channel 24 was dead. To minimize the effect of this lost channel, sensor 23 was moved to the location originally designated for sensor 24. The spacing for the two transducers mounted on the tip of the blade was thus increased to 57.0 in. (144 cm). This change of position significantly decreases the sensitivity of the measurements in the tip of the blade. As the blade was not expected to fail in this region, the selection of this array pattern for the sensors minimized the effect of the loss of channel 24. Figure 19b shows the final positions of transducers 13 through 23.

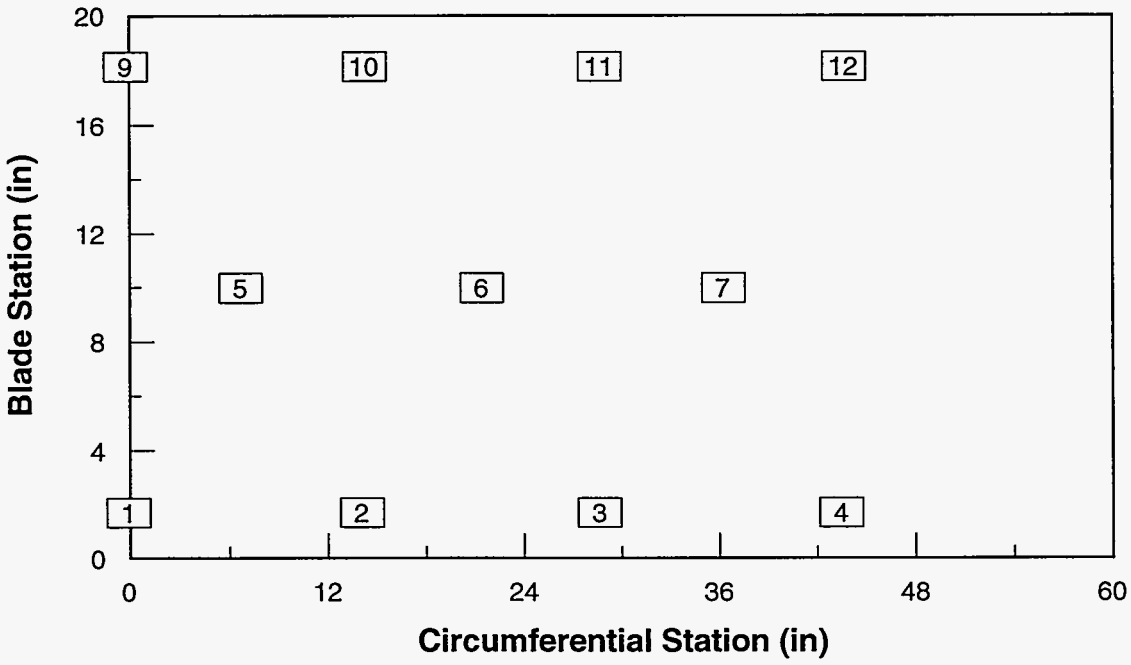

Figure 19a. Blade root.

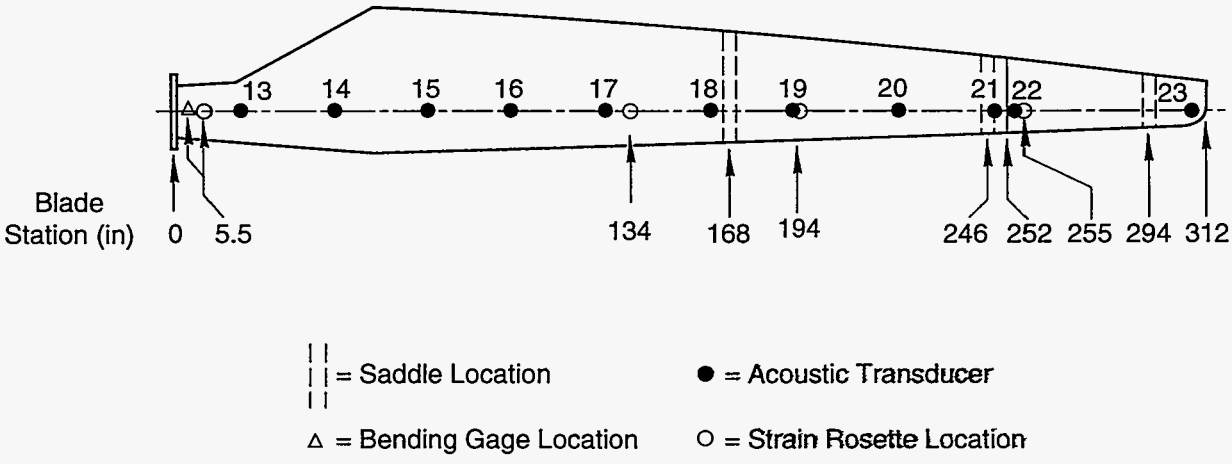

Figure 19b. Blade span.

Figure 19. Schematic diagram of the AE sensor locations.

3.2.5 Data Acquisition and Analysis

To provide a coordinated event record of the AE events, the output of a load cell was recorded by the system every half second (0.5 sec). The primary parameters recorded in the data set were time of occurrence (to 0.125 μsec), sensor number, signal rise time, AE count, signal duration, peak amplitude and "energy." The energy parameter used here is the area under the voltage-time curve of the burst instead of the true signal energy; i.e., the area under the voltage squared-time curve. An "AE count" is the number of times the acoustic signal crosses a preset threshold. This set of parameters was stored on the hard disk of the system for most of the signals detected. The system was set to ignore signals with under three counts or a duration less than 100 microseconds. Signals with one or two counts are often random noise, and signals under 100 microseconds are usually electromagnetic noise.

During the test, a real-time plot of the number and location of AE events was displayed by the system. Post-test analyses of the data were performed to permit a more detailed examination of the measured data.

3.3 Real-Time Test Results

3.3.1 Phase 1

Figure 20a is the "location plot" for the AE events in the root of the blade during Phase 1 loading of the blade. As can be seen in these plots, most of the emissions came from the compression side (top) of the blade, between transducers 9 and 12. As seen in this plot, the events were located primarily between blade stations 12 to 20. Figure 20b shows a similar plot along the length of the blade. There was a small cluster of events between stations 40 and 55, near sensor 14. Most of the events were from a region near station 240 (between sensors 20 and 21).

Figure 21a shows the AE events in the root of the blade plotted as a function of the load on the blade. In this plot, the number of AE events for transducers 1 through 12 is summed together to get the total number of events emanating from the root of the blade. The large number of events noted in this figure implies that significant damage may be accumulating in the root of the blade. However, the location graph, Figure 20a, illustrates that the damage is

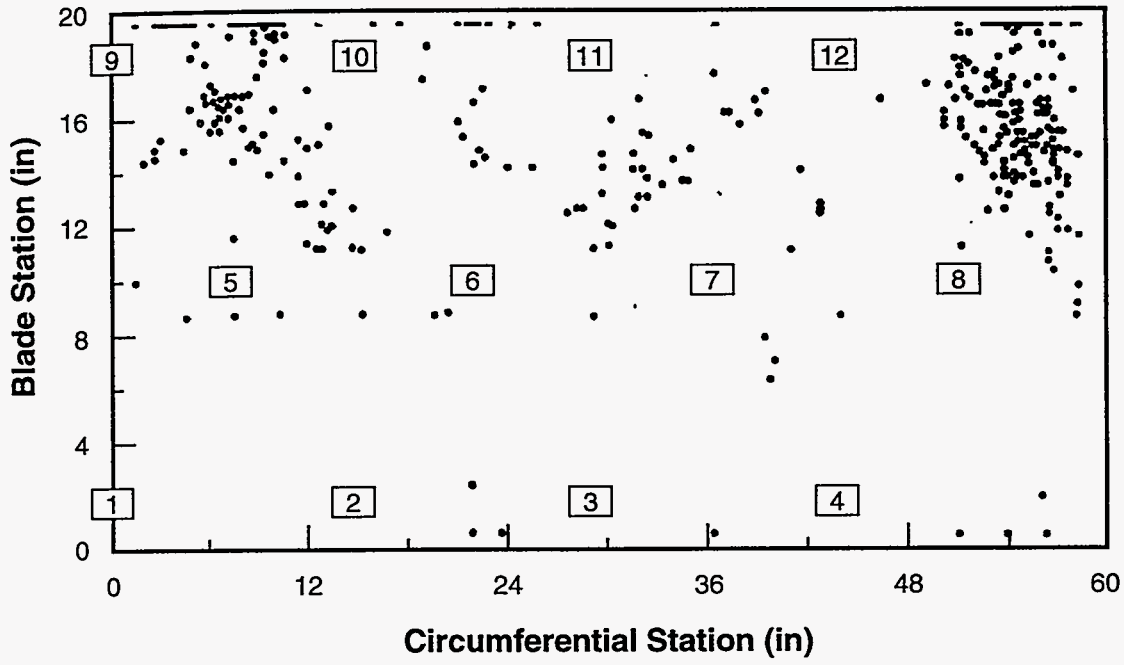

Figure 20a. Root region.

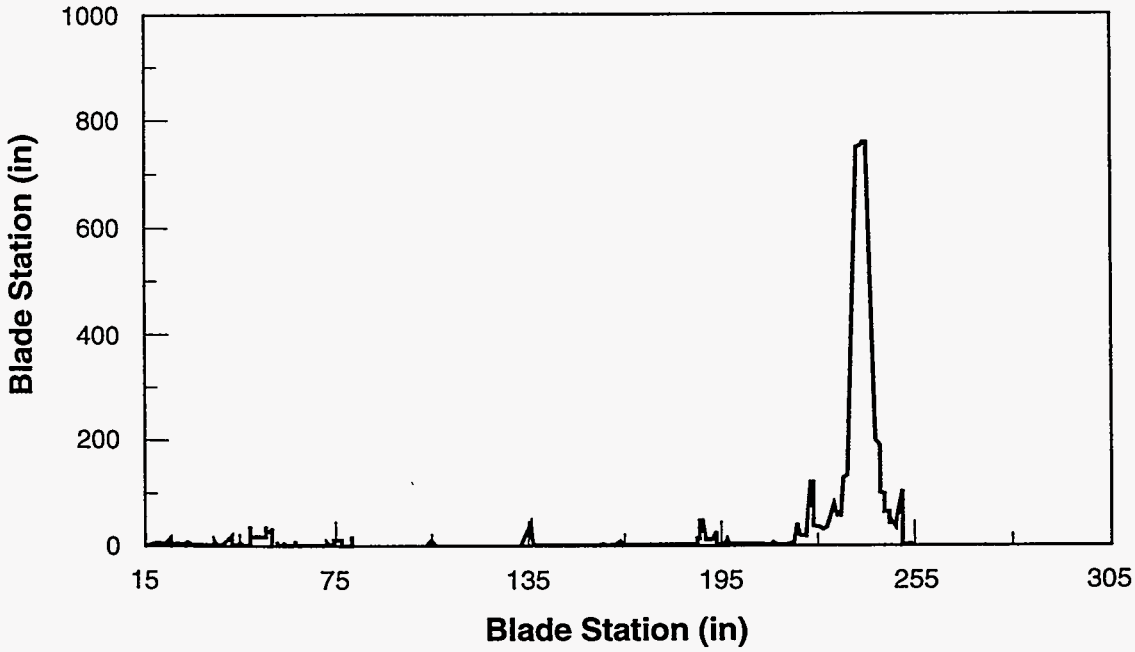

Figure 20b. Blade region.

Figure 20. AE locations for Phase 1 loading.

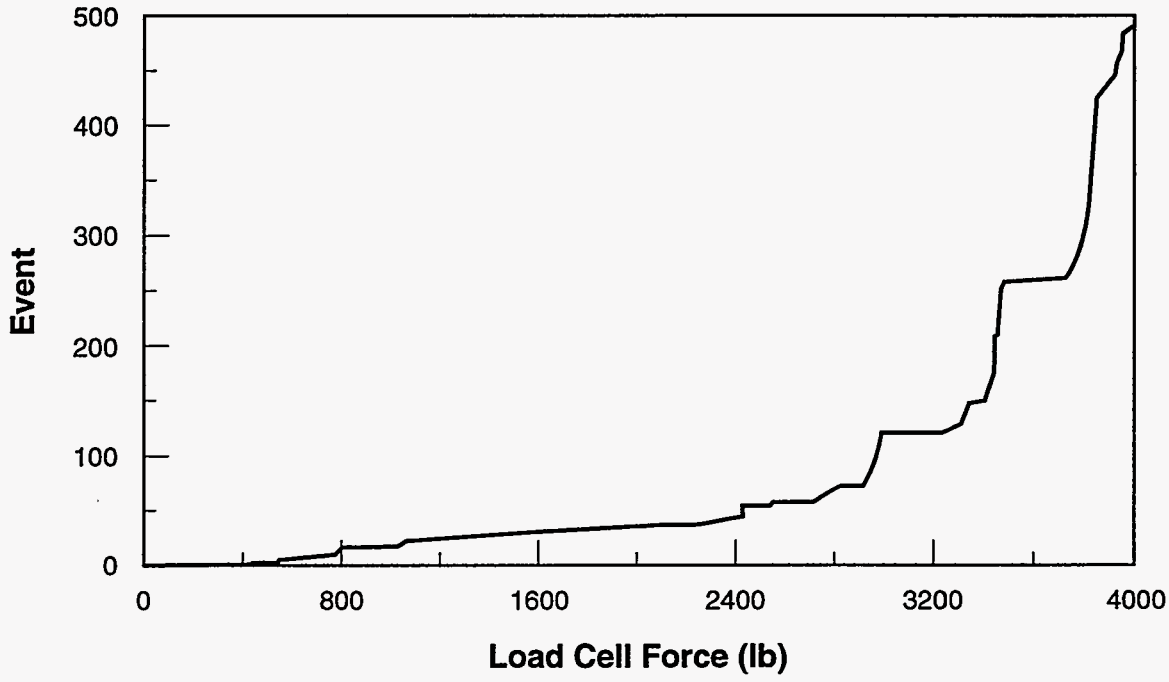

Figure 21a. Root region.

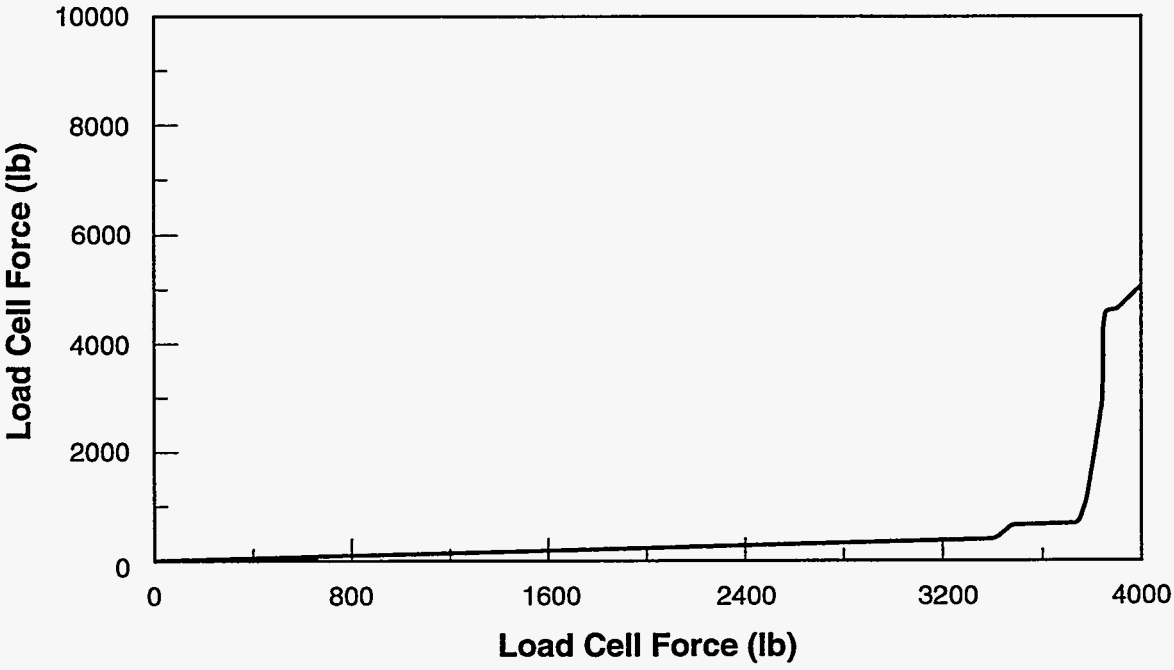

Figure 21b. Blade region.

Figure 21. AE events for Phase 1 loading.

widespread and not concentrated into a few serious flaws. Figure 21b shows the events versus load curve along the span of the blade; i.e., the AE events from transducers 13 through 23 are summed together. This plot indicates that the onset of failure started at about 2900 lb (12.9 kN) load; i.e., most of the AE events occur during the load step. As shown in Figure 20b, most of these AE events were clustered at or near the blade failure zone between stations 240 and 250.

3.3.2 Phase 2a

Figure 22a shows the load versus time curve for the Phase 2a loading. This an expansion of Figure 6b to show more detail. Figure 22b shows the cumulative AE events in the root of the blades. The time history plot shown in Figure 22b presents an incorrect view of the AE events. The problems associated with this figure are discussed in more detail in the post test analysis.

The root location plot is shown in Figure 23a. This figure is similar in appearance to Figure 20a, which shows the locations for this region during the Phase 1 loading. This figure shows continuing widespread damage and it indicates that flaws are coalescing into cracks and growing. The main difference between the two figures is the appearance of lines of located events near sensors 8 and 12. Both the vertical and horizontal lines shown in Figure 23a are artifacts of the location algorithm.*

Figure 23b shows the location graph for the blade region for Phase 2a loading. The emission near blade station 15, sensor 13, is an extension of damage seen in the root region. The events near station 50, sensor 14, are a continuation of the damage seen in Figures 20b. Note that the number of emissions from this area in the two figures is approximately the same. The emissions just beyond station 165, sensor 18, are emanating from the load fixture (saddle). As this fixture is being used to supply the entire load on the blade (one saddle instead of three), the bottom of the blade was beginning to crush.

* As noted in [2], straight lines in a location plot may be indicative of an artifact of the location algorithm. To determine if these lines are indeed artifacts, the scale of the plot is greatly expanded. If the points still fall on a straight line when the horizontal scale is expanded, then one knows that the points in the line are not plotted correctly by the location algorithm, e.g., when the scale is expanded from 5 in/cm to 1/10 in/cm.

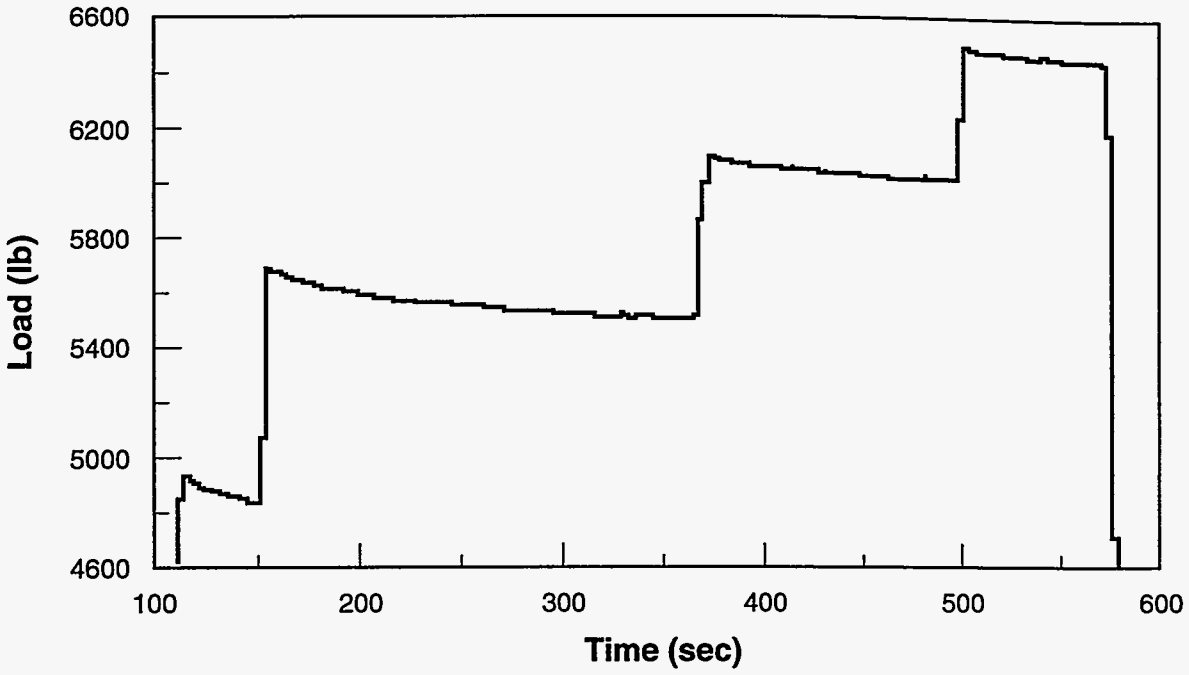

Figure 22a. Load history.

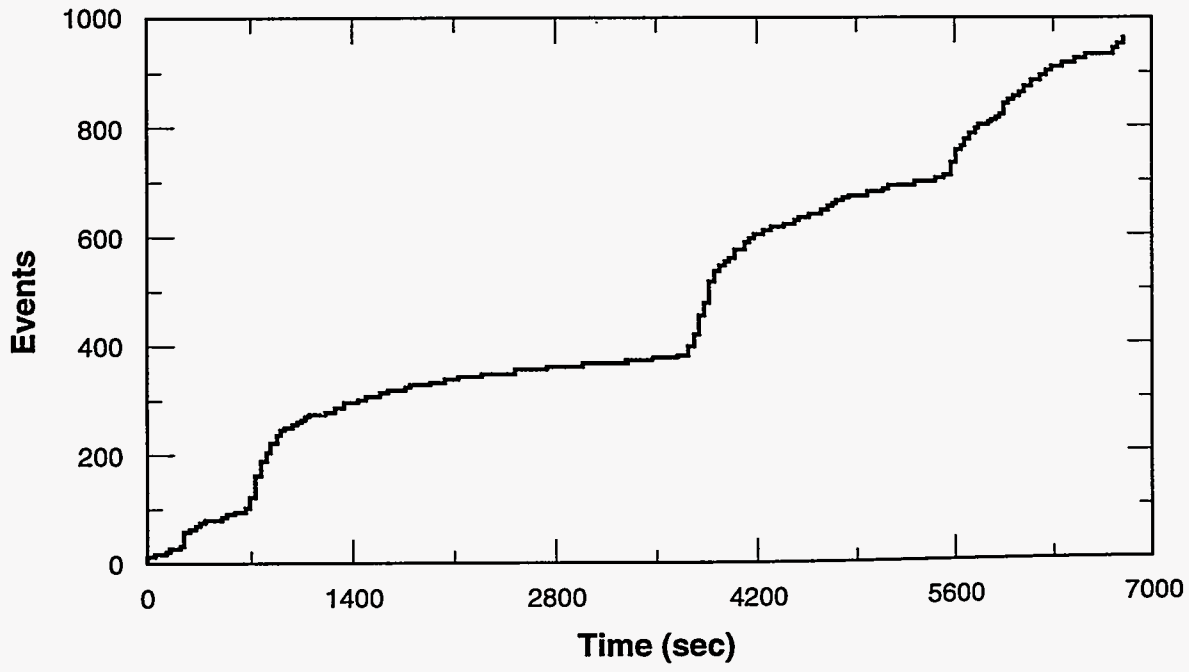

Figure 22b. Root region.

Figure 22. Time histories for Phase 2a loading.

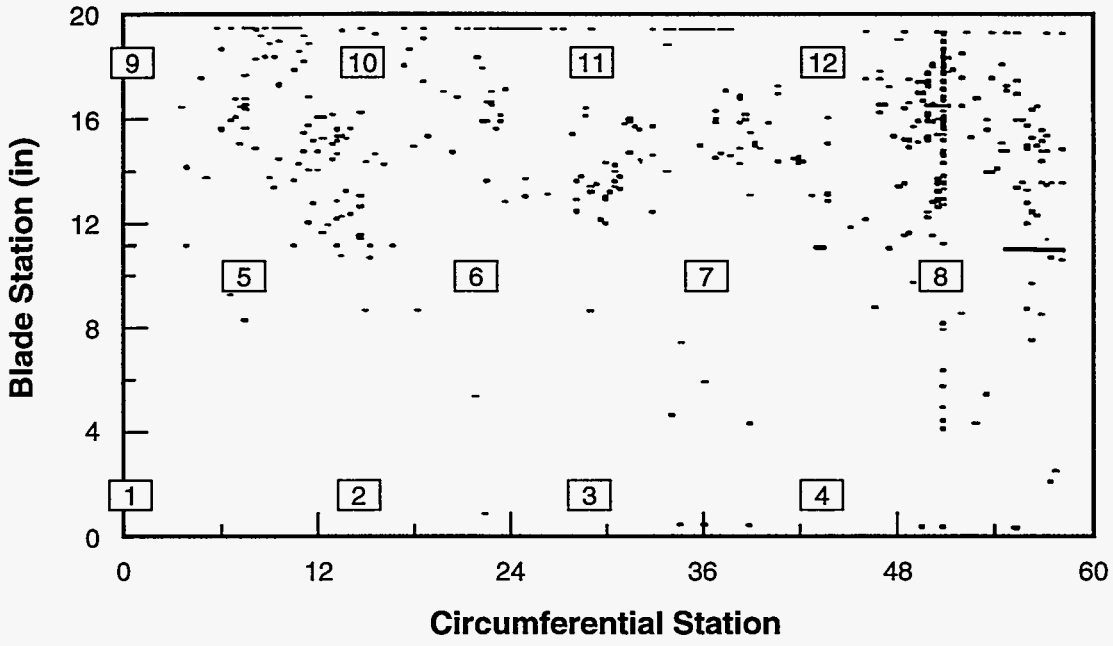

Figure 23a. Root region.

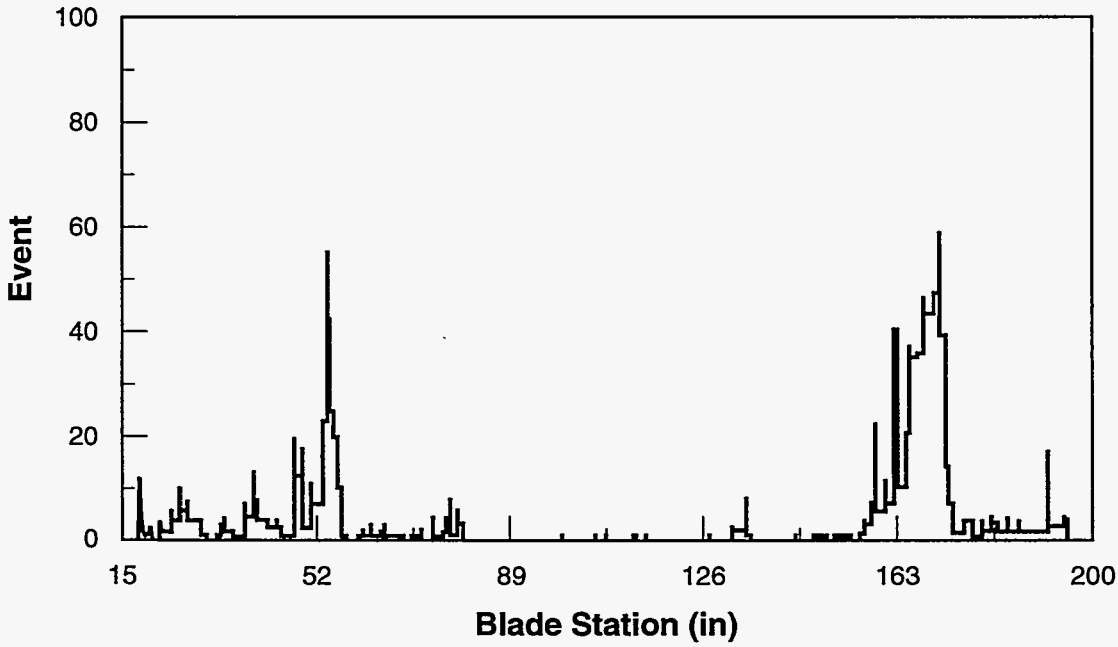

Figure 23b. Blade region.

Figure 23. AE locations for Phase 2a loading.

Figures 24a and 24b are the AE event plots for Phase 2a loading. They show that while there was significant emission at each load increase, there was more during the periods of the load hold while the load was decreasing.

3.3.3 Phase 2b

Figures 25a, 25b and 25c are the event-time plots for the blade root for the Phase 2b loading. An expanded plot of the load-time history for this loading sequence (Figure 6c) is provided for reference in this plot as Figure 25a. The time history for the root region of the blade is shown in Figure 25b and the blade region is shown in Figure 25c. The location plots for this load sequence are given in Figure 26. Figure 26a is different from previous plots in that the scales have been expanded. The figure covers only the top of the blade, from blade stations 10 to 20, and sensor 9 is located in the center of the plot. Two areas of massive damage are seen: one above sensor 8 and the other below sensor 9. The diverse nature of these data indicates that the damage is not the result of the growth of several flaws; rather, the damage appears to be a massive disintegration of the fiberglass with some fiber breakage as well.

Figure 25b shows the events as a function of time for the root region of the blade. Notice that while there is some increase in the event rate during the loading, there are even more emissions for the loads above 7300 lb (32.5 kN), at approximately 480 seconds, right after a step in the load. This observation is indicative of a rapid increase of blade damage. The accumulation of damage slows as the stress is redistributed and the load drops. This figure also shows that there was steady damage growth between all load steps. Thus, blade failure probably would have occurred in this region for all loads above 6000 lb (26.7 kN), if the loads were held long enough.

As discussed above, the straight lines of points shown in Figure 26a are artifacts of the algorithm used to locate the AE events.

In Figure 26b, the damage near station 50 continues for this loading sequence, and the breakup of the blade bottom under the loading fixture near station 170 is still obvious. Figure 25c shows the event versus time curve for this region. There was not as much damage occurring during the load holds here as there was in the root region.

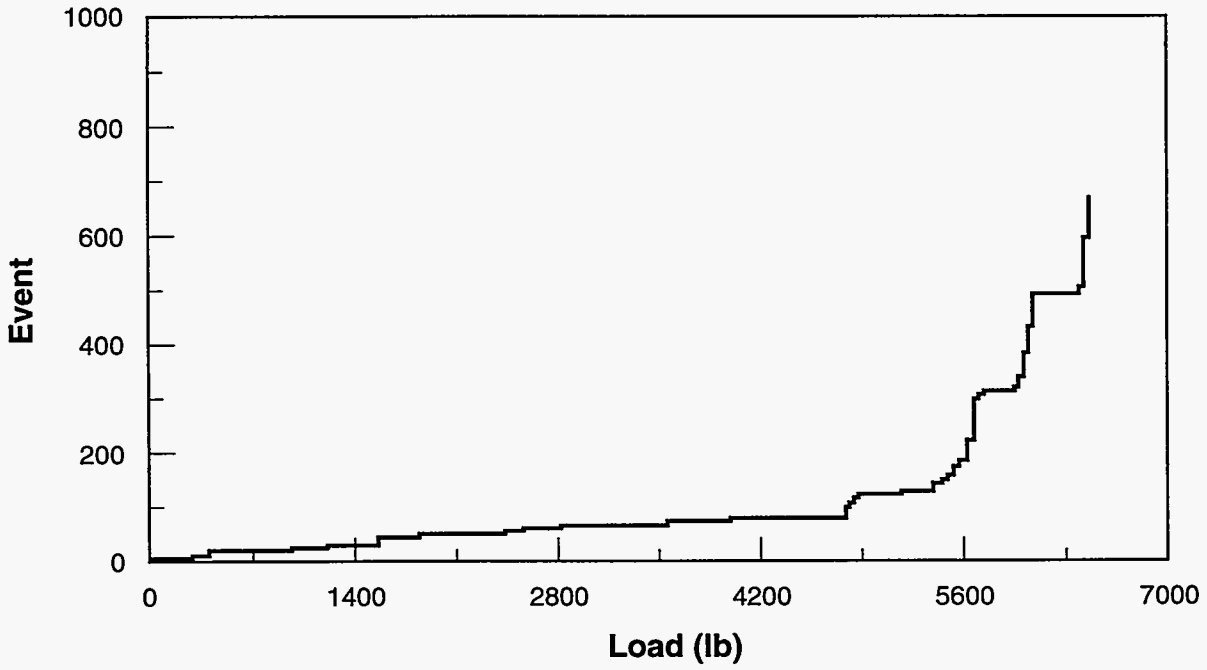

Figure 24a. Root region.

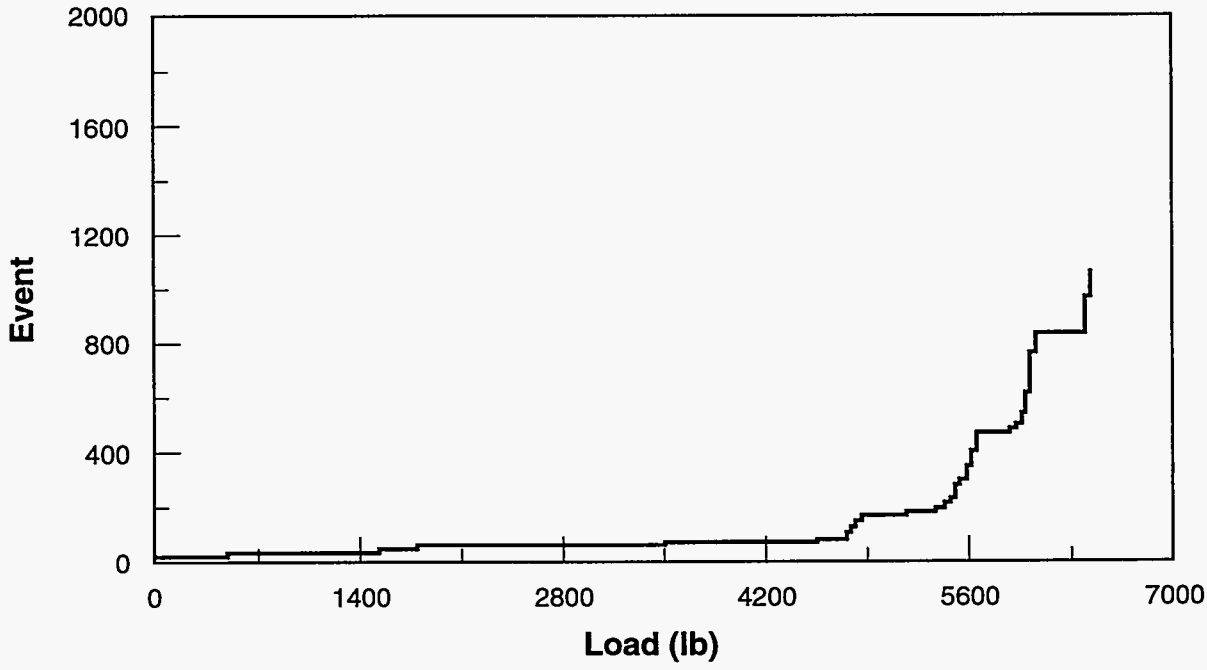

Figure 24b. Blade region.

Figure 24. AE events for Phase 2a loading.

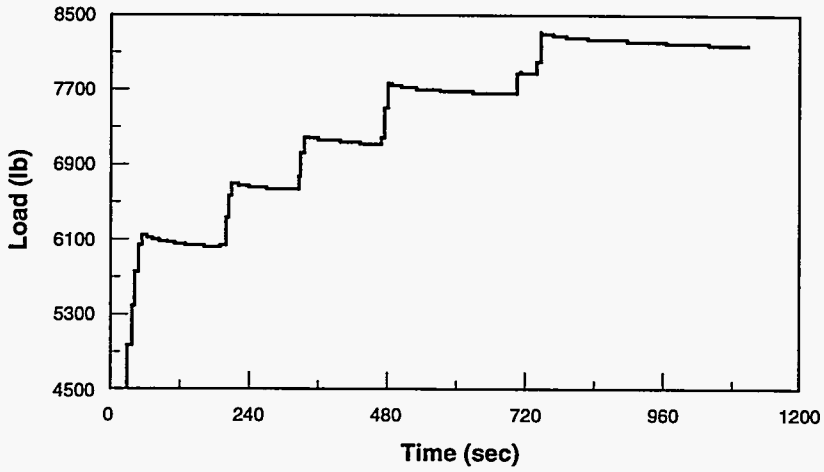

Figure 25a. Load history.

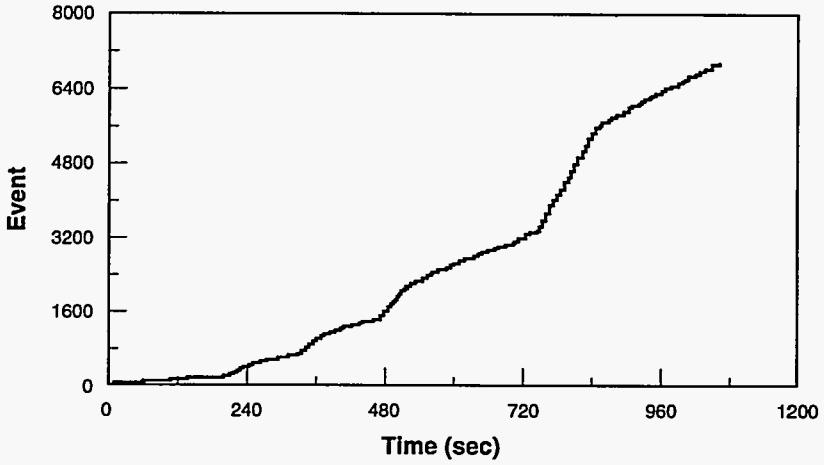

Figure 25b. Root region.

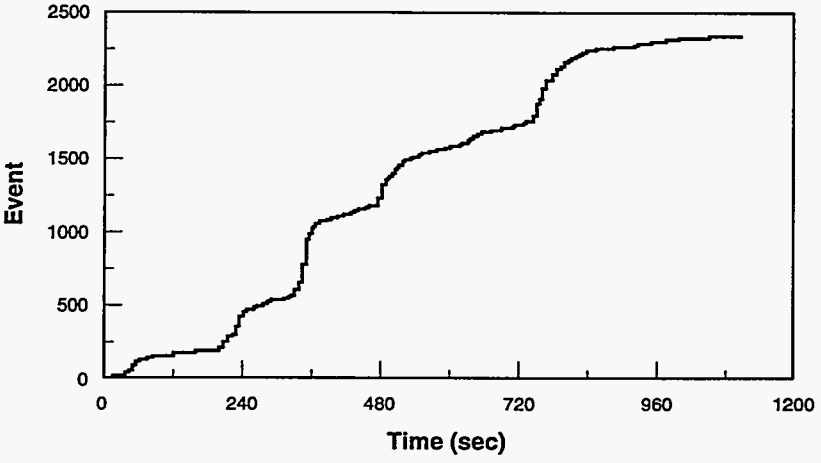

Figure 25c. Blade region.

Figure 25. Time histories for Phase 2a loading.

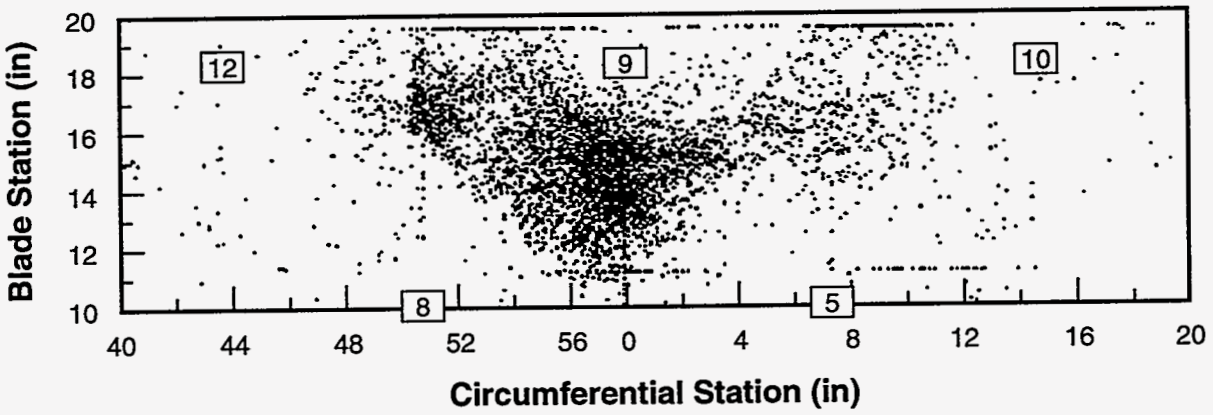

Figure 26a. Root region.

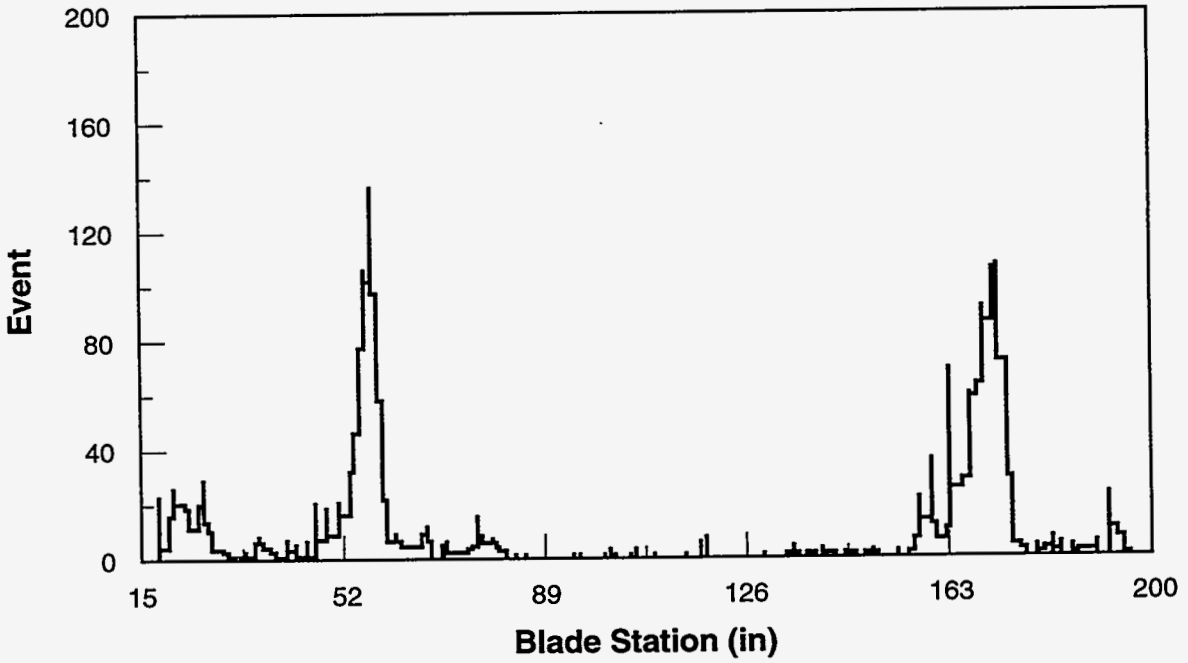

Figure 26b. Blade region.

Figure 26. AE locations for Phase 2b loading.

3.4 Post-Test Analysis

3.4.1 Root Region

For Phase 1 and 2a loadings (see Figures 20a and 23a), there was, more or less, a random scattering of located events in the root region. Most of the events were in the band that lies between blade stations 12 and 20. In this band, there was some concentration of AE events on the top of the blade and toward the leading edge. Sensor 9 (see Figure 19a) recorded the most AE events, but all of the sensors in the root region detected emissions. The total number of hits in the Phase 1 and 2a loadings ranged from 287 on sensor 3 to 2,625 on sensor 9. Figures 27a and 27b are plots of the total "energy" for the emissions detected by sensor 9 during Phase 1 and 2a loadings, respectively. In these plots, all events whose rise time was greater than one half the signal duration were ignored. These were mainly low amplitude emissions with signal characteristics that resemble noise more than acoustic emission. In these figures, the energy increases after a load step for all loads above 2900 lb (12.9 kN). If acoustic emissions do not cease almost immediately after a step in the load, then either a flaw is growing or, in this case, the stress level in the blade structure has exceeded the strength of the fiberglass. The location graphs (Figures 20 and 23) show that the damage is spread over a wide area in, more or less, a random fashion.

The location map for Phase 2b loading (Figure 26a and 28) shows large scale destruction of the fiberglass. Figure 27c is the "energy" versus load curve for sensor 9 during this loading sequence. The amount of emission "energy" increases during each load hold. Most of this "energy" comes from the compression side (top) of the blade. The most probable failure mechanism is delamination of the fiberglass. In Figure 28, there is only a slight concentration of events in the triangle formed by sensors 6, 7, and 11. This area is in tension. The conclusion is that the fiberglass structure in the root region still has adequate strength under tension at the 8996 lb (40.0 kN) load [peak root bending moment of 125,944 ft-lb (170 kN-m)] but cannot support the compression stresses without damage above a load of 3925 lb (17.5 kN) [root bending load of 72,528 ft-lb (97.9 kN-m)] seen on the first loading.

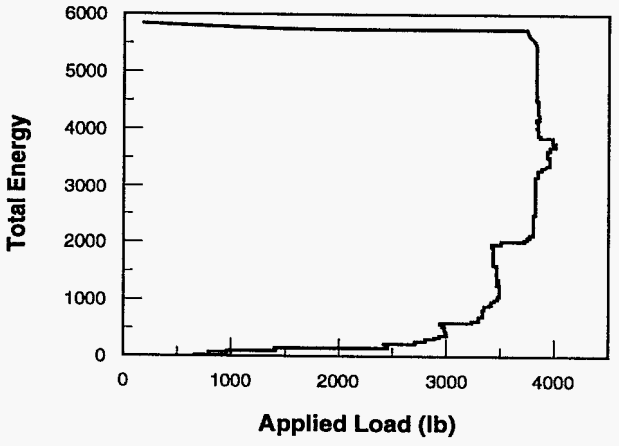

Figure 27a. Phase 1 loading.

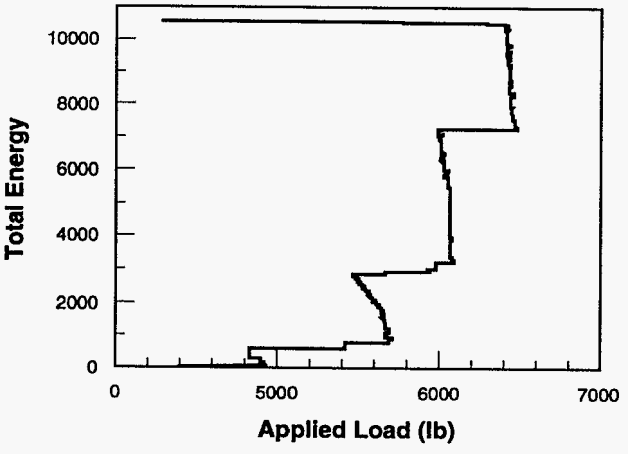

Figure 27b. Phase 2a loading.

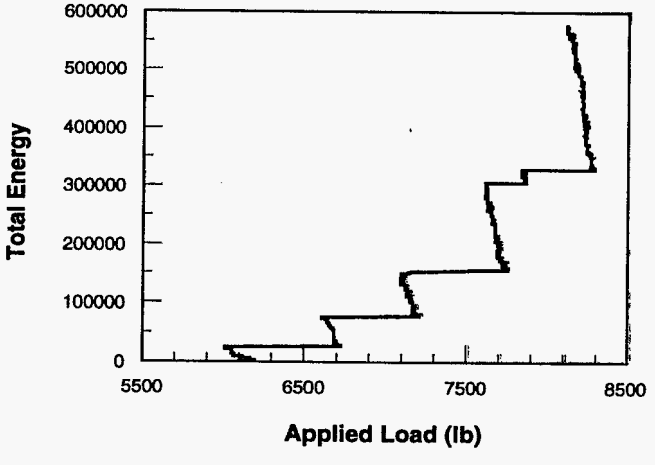

Figure 27c. Phase 2b loading.

Figure 27. Total "energy" for sensor 9.

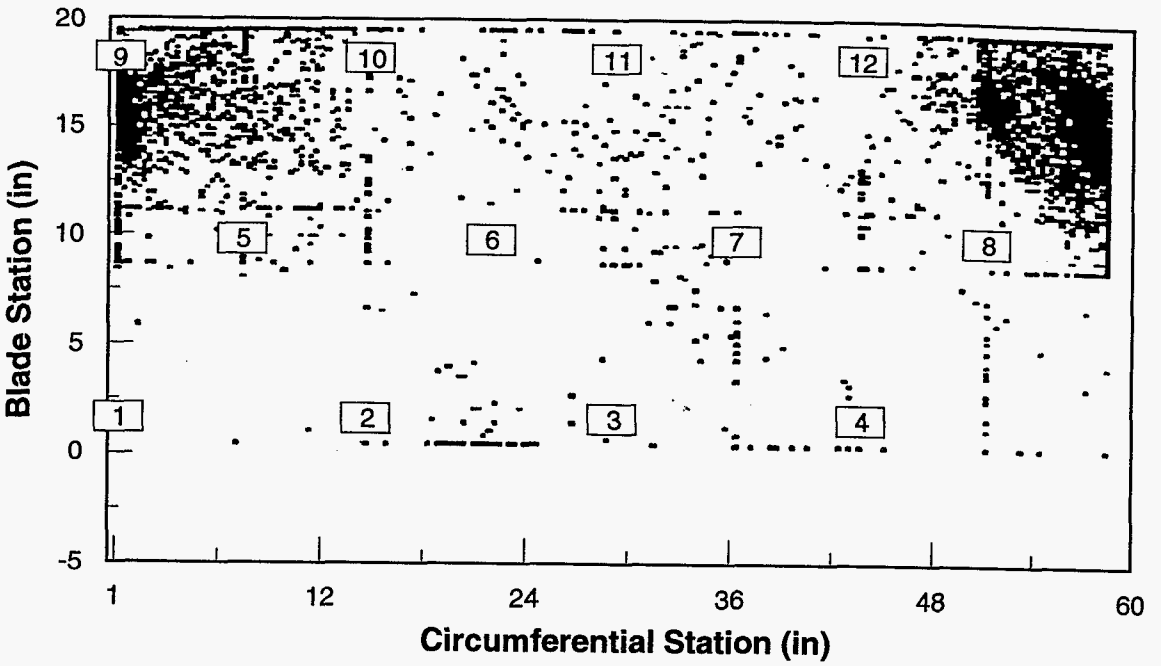

Figure 28. AE locations for Phase 1 loading of the root region.

3.4.2 Blade Region

Phase 1 loading produced a failure in the blade near the tip. The location plot for blade during this load cycle (Figure 20b) shows two regions with a clustering of event locations. One is between stations 40 and 56 and the second is between stations 234 and 242. Expanded location plots for these two regions are shown in Figures 29a and 29b. The events shown in Figure 29a started very early in the loading and continued at a moderate level for all three loadings. Figure 30 shows the acoustic "energy" detected at sensor 14 (station 48) versus the load for the three different loadings. For Phase 1 loading, there is more "energy" emitted during the increasing load than during load holds. However on each load hold over 4800 lb (21.4 kN), there is more "energy" emitted during the hold than during the loading, although the amount of emitted "energy" decreases after the hold at 7100 lb (31.6 kN). The emitting structure between stations 40 and 56 appeared to be reaching a point where all the material which could break, had broken and the rest was still capable of bearing the load at 8996 lb (40.0 kN). Upon sectioning of the blade in this region, it was found that one side of the box spar, which started at about station 37 and then ran most of the rest of the length of the blade, was debonded from the top skin in the region from station 37 to about station 50. Also found was a section of the skin on the top of the blade, about 5 in. (127 cm) wide and running from about station 37 to station 54, which was only

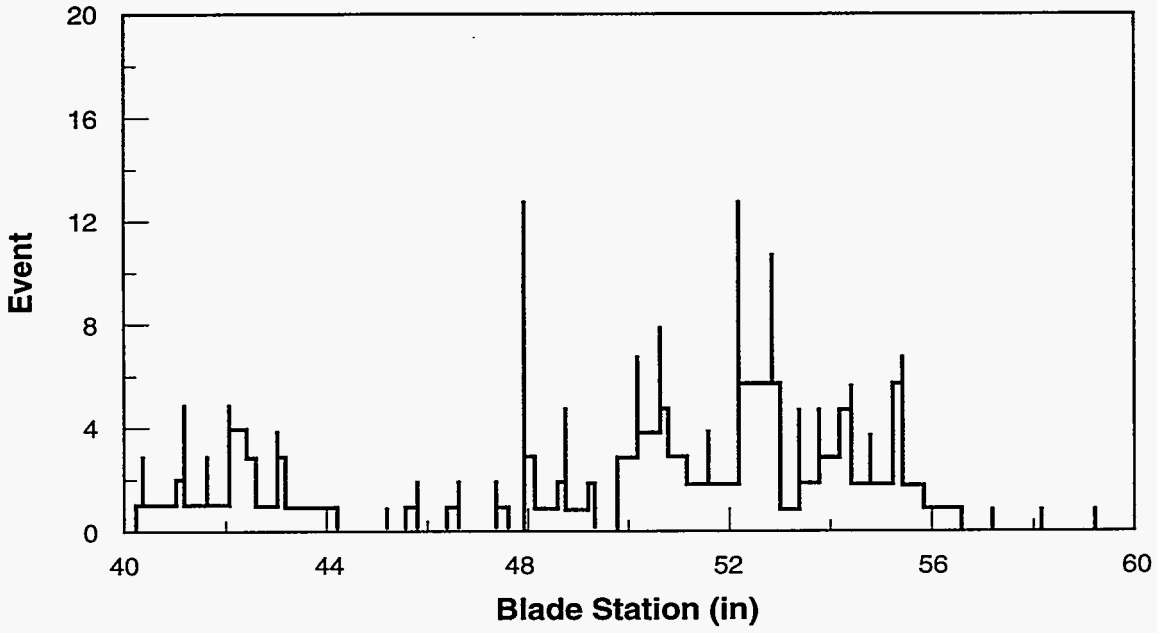

Figure 29a. Station 40 to station 60.

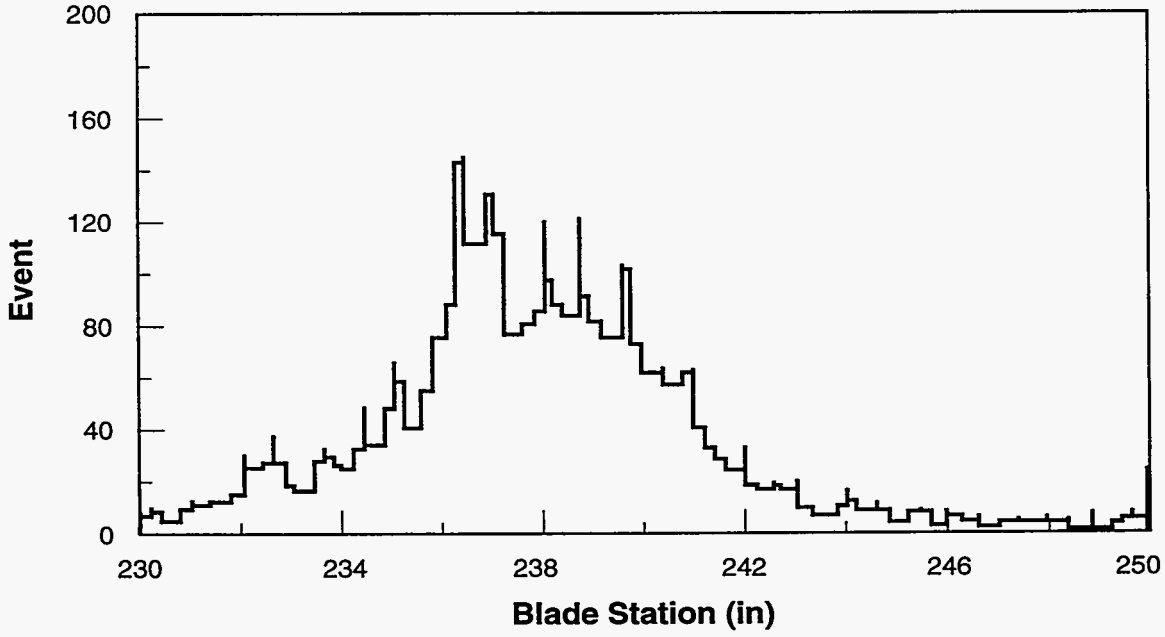

Figure 29b. Station 230 to station 250.

Figure 29. AE locations for Phase 1 loading.

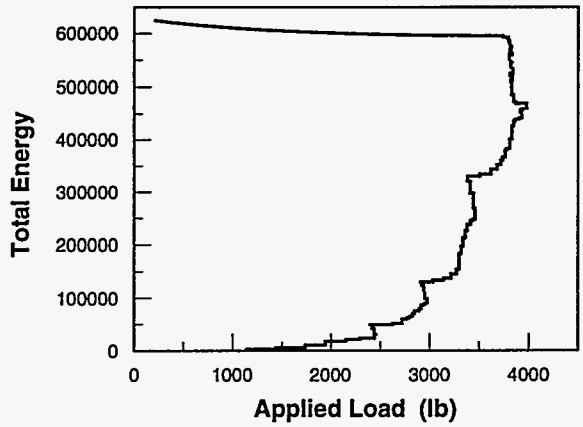

Figure 30a. Phase 1 loading.

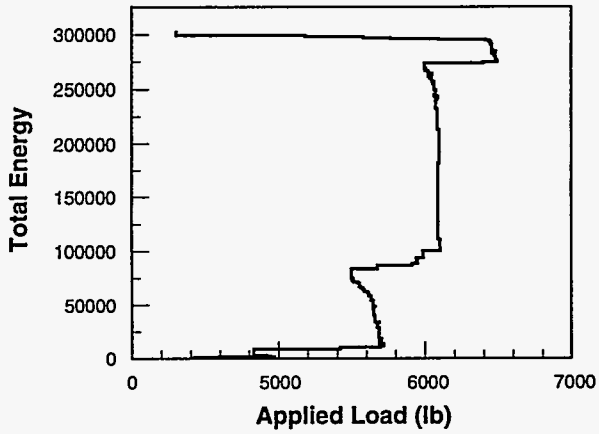

Figure 30b. Phase 2a loading.

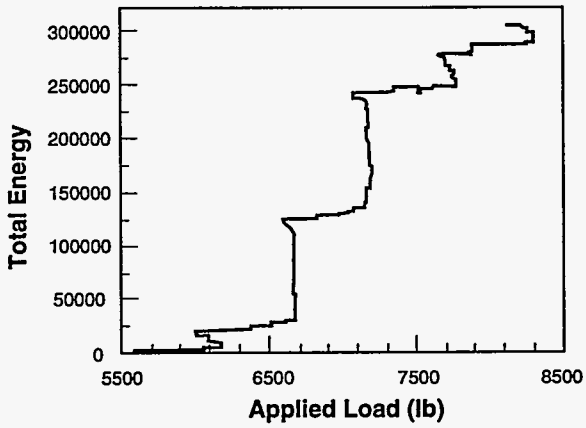

Figure 30c. Phase 2b loading.

Figure 30. Total "energy" observed by sensor 14.

about one half the thickness of the rest of the skin in this area. The emissions observed in Figures 20b, 23b and 26b most probably come from the progressive debonding of the spar from the top skin. However it is possible that the thinned skin underwent some buckling and produced some of these emissions. A further examination of Figure 30 reveals that almost half of the energy emitted from this region occurred during the Phase 1 loads above 2400 lb. Relatively few of the emissions occurred at loads above 7200 lb.

Figure 31 is the "energy" versus load curve for sensor 21 (station 250) during Phase 1 loading. This data is basically the "energy" for the events shown Figure 21b. Here the first emission is observed at 2800 lb (12.5 kN). Appreciable emissions begin during the load hold at 3500 lb (15.6 kN). Failure starts at approximately 3400 lb (15.1 kN) and continues to 3925 lb (17.5 kN). At this point there is a load drop, indicating structural failure, followed by large amounts of emissions, which was probably produced by tearing of the upper skin. Examining the sectioned blade, debonding of the strengthening web from the top skin was found from about station 230 to its end at station 239. There was also buckling and tearing of the top skin between stations 236 and 242. This is exactly the region of failure located in Figure 21b. Also shown in this figure is that almost no emissions emanated from this region for loads below 2800 lb (12.5 kN). During the Phase 2 loading, considerable emissions were detected in the region from station 155 to station 175; see Figure 32. The emissions from stations 163 to 175 are primarily caused by the bottom surface breaking up under the loading fixture. However this does not account for the events observed between stations 157 and 161.

Figure 33 shows the detected acoustic "energy" from sensor 18 versus the load for phase 2 loading. Most of this energy comes from the breakup of the skin caused by the loading fixture. The blade was not sectioned in this region, but a piece from stations 132 to 138 shows debonding of the box spar from both the top and bottom skins. It is probable that such debonding was present along much of the blade during this loading. While this loading broke the blade with appreciable violence, the acoustic emission pulse associated with this failure has not been identified. The failure appeared to start near the trailing edge of the blade and the foam inserts could have damped the wave to the point where it was indistinguishable from other emissions. There was also bond failure between the top and bottom skins at the leading edge.

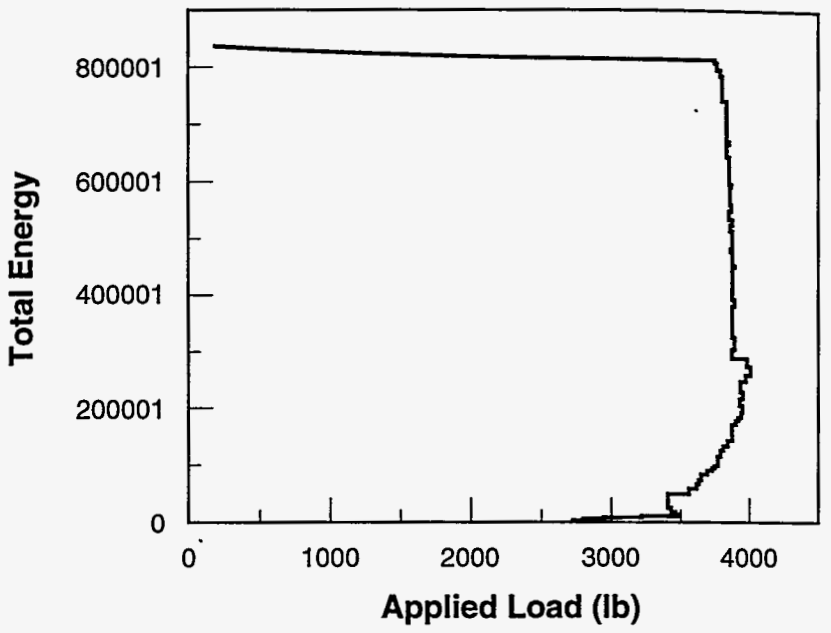

Figure 31. Total "energy" observed by sensor 21 during Phase 1 loading.

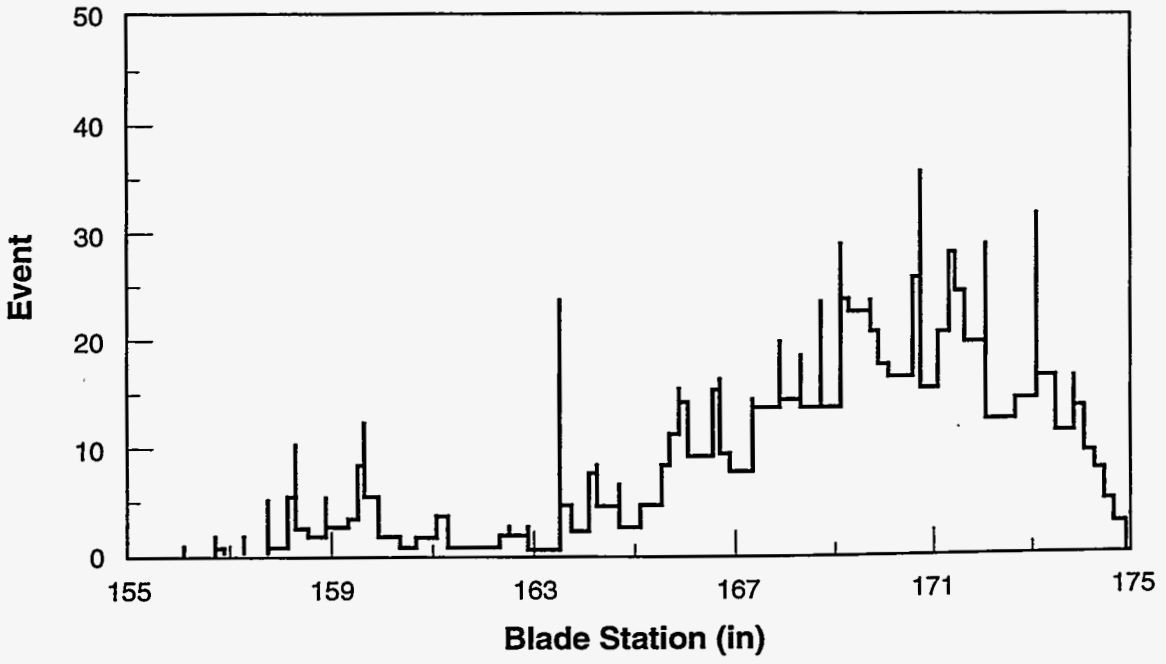

Figure 32. AE locations for Phase 1 loading between stations 155 and 175.

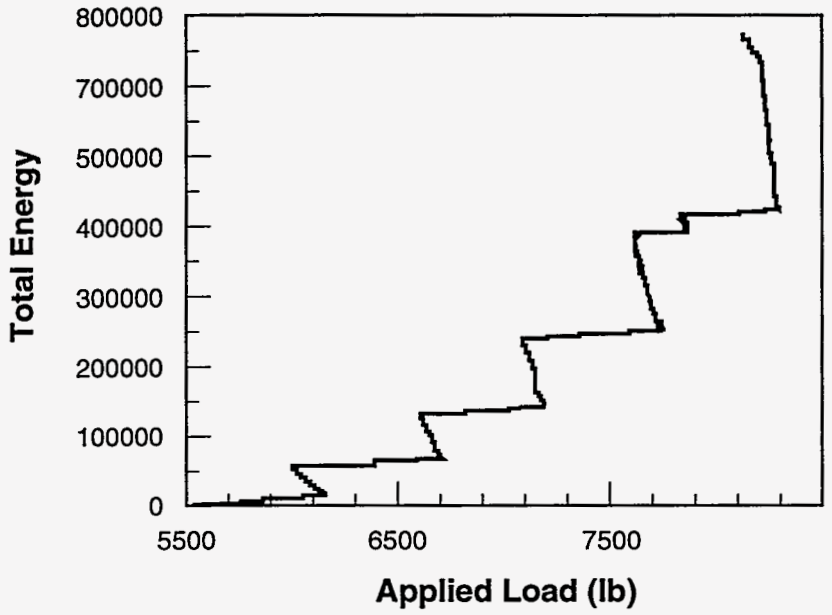

Figure 33. Total "energy" observed by sensor 18 during Phase 2b loading.

3.5 Discussion

The acoustic emission test clearly detected the primary blade failure near station 240 and showed that there was little damage in this region until the load exceeded 15.1 kN (3400 lb). The debonding of the rear spar near station 37 was seen to start at a load of 10.7 kN (2400 lb). The debond propagated outward as the load was increased until it finally stopped around station 56. This damage did not have a significant effect during these overload tests but may have led to a long-term fatigue failure in actual service.

The real time data observed the buildup of damage at the locations well before blade failure. Thus, AE can be used to detect "hot spots" or "weak points" in the structure before it fails. For the failure at station 240, the AE events marked this area at a load of 15.1 kN (3400 lb) or approximately 95 percent of the ultimate load. For station 37, the area was located at a 10.7 kN (2400 lb) load or approximately 67 percent of the ultimate load. In both cases, the blade could have been unloaded before catastrophic failure occurred.

4. THE COHERENT OPTICAL TECHNIQUE

4.1 Technique Description

The measurement category of "coherent optics" covers a broad range of interferometric techniques including single-point interferometry, holographic interferometry (holometry), electronic speckle pattern interferometry (ESPI) and shearography [3]. All of these techniques use the wavelength of light as a base metric, and an interference geometry of some sort to make the actual measurement. In other words, in all these interferometric techniques, light is bounced or scattered off an object of interest. As the object moves, the distance the light travels (the optical path) changes, and this modifies the phase of the scattered light. This light is then combined with another light beam of the same wavelength (a reference or undisturbed beam) to produce optical interference, which converts the optical phase into intensity variations, which can be measured. Holometry, ESPI, and shearography are all "wide area" or imaging techniques, where the interference manifests as dark fringes superimposed on an image of the object under test. Typical sensitivity to surface displacement is a few microns.

The technique used for this test was shearography. In shearography, the reference beam is derived from the object, by "shearing" the image--that is, by producing two images, slightly shifted relative to one another. This results in interferometrically comparing motion at two nearby points, which actually gives a measurement of surface slope. The major advantage of shearography over the other configurations is its tolerance of object motion. Since the test and reference beams follow nearly common paths, it is insensitive to fairly large motions of the test object relative to the optical system, while still able to detect local anomalies or deformations. While holometry and ESPI require careful vibration isolation, shearography is much more suitable for a field test such as this one. One disadvantage of shearography is that quantitative displacement analysis is somewhat more difficult than in ESPI or holometry. The major use of shearography has been in flaw *localization* as opposed to quantitative displacement analysis, and that was how it was used for this experiment.

4.2 Experimental Setup

The system used for this test was the United Technologies Pratt & Whitney (P&W) electronic holography/shearography inspection system (EHIS/ESIS). This is an "open" system,

capable of being configured for either ESPI or shearography. The particular system consisted of an optical head supported by a tripod, and a separate six foot rack of electronics containing the digital image processor, computer, video display and hard copy and other support electronics. For the pre-test inspection, the blade was oriented with the chord vertical, as shown in Figure 34. This arrangement was selected for convenience in positioning the optical head. The compression side of the blade (the top of the blade during the test) was inspected in 12 in. (0.3 m) increments. The entire surface of the blade root was also inspected. For the real-time and post-test inspections, the blade was supported in the as-tested configuration; see Figure 35. Selected sections of the blade and the root were inspected during these two test phases.

Thermal stressing (a heat gun is used to thermally stress the blade) was chosen for the pre-test and post-test inspection for its combination of convenience and sensitivity to debonds and delaminations, which were assumed to be the most likely flaws in this type of construction. These flaws have both a lower thermal conductivity and lower mechanical stiffness, so under thermal stress the debonded area tends to bulge out from the surrounding surface. Laboratory tests of debond detection in similar composite structures with thermal stress indicate a sensitivity to flaws of 1 in. (2.5 cm) in diameter.

Differential loads were used for the real time inspections. For each step in the loading sequence described above, the blade load was allowed to decay slightly during a relatively short hold period. The optical inspections were performed during this varying load condition.

The primary data output of this system is a live video image of the interference fringes. By either allowing the part under test to move slowly (in this case by cooling), or by introducing an intentional phase shift in one of the optical beams, fringes can be observed moving over the area of interest. This fringe motion makes flaws and discontinuities much more visible than they are in static photographs of the fringe fields [3]. Three methods of recording data were used: video hard copy of fringe images, a videotape of the moving fringe images, and marking suspect areas on the blade surface while viewing the live fringes. The latter method is the easiest to relate to the actual blade geometry and is the primary method used to relate the shearography results to the post-mortem dissection of the blade. A digital image archive would have been desirable. This would have allowed the static interferograms to be processed for best display, rather than relying on the video hard copy for archiving the data. However, the system used here does not have that capability.

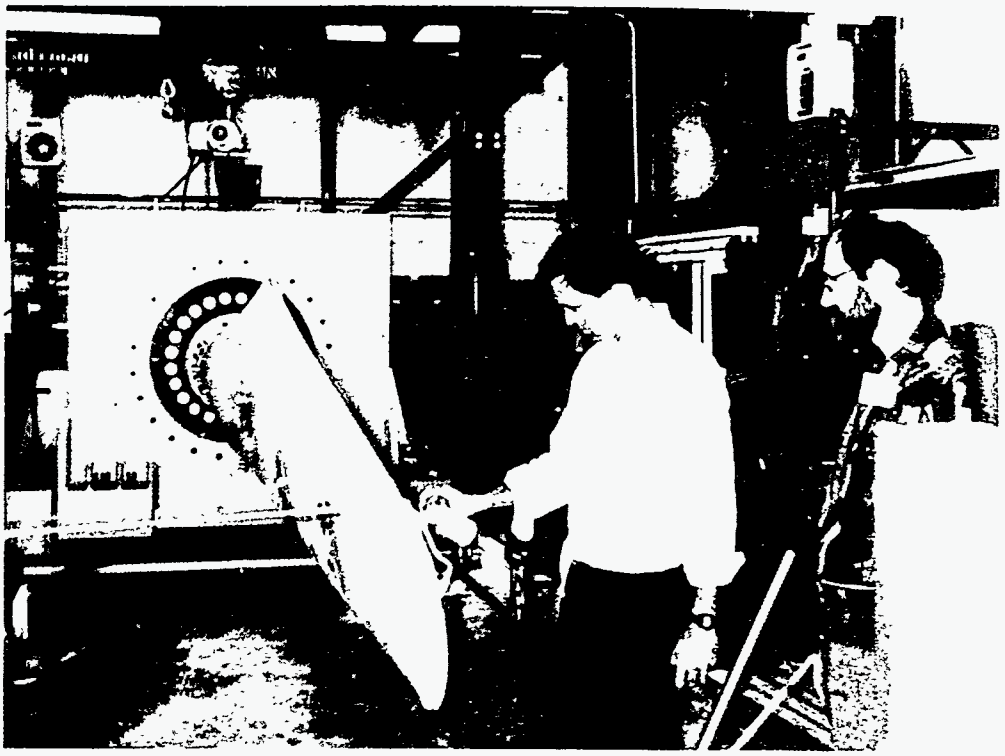

Figure 34. The shearography system viewing the compression side of the blade.

Figure 35. The shearography system viewing the root section of the blade.

4.3 Results

4.3.1 Pre-Test Results

For the pre-test inspection, the blade was mounted with the chord vertically, and the optical system was arranged to view the blade from a position essentially level with the area under inspection. Natural vibrations of the blade, caused by acoustic noise, wind, etc., made it impossible to take data over most of the blade surface due to gross motion, so a rope, visible in Figure 34, was tied to the end of the blade to damp and stiffen the system.* A flat white powder (dye penetrant developer) was sprayed on the blade to lessen the specular reflections, which caused hot spots in the image. A viewing area of approximately 11.5 in. (29.2 cm) vertical by 14.5 in. (36.8 cm) horizontal was selected, and views were taken at 12 in. (30.5 cm) increments horizontally to provide some overlap between views. A total of 39 views was taken of the blade low pressure surface, concentrating on the spar and other underlying structure. Another 16 views were used to inspect the entire surface of the blade root.

For each inspection view, the optical system was positioned, and a reference frame was stored. The view area on the blade was then heated with a hot air gun, and the resulting deformations were observed in real time. When the fringes had developed to a degree judged reasonable by the experimenters, the fringe image was frozen, and a video hard copy made. No digital recordings of the images were kept.

In fact, very few obvious flaws were detected on this blade by coherent optics. Various subsurface structure such as the spar webs and lamination thickness changes were readily visible, as shown in Figure 36. This shearograph highlights the tip actuator mechanism and the main spar, between stations 240 and 252 in Figure 19b. Several anomalous areas, as well as the apparent substructure, were marked on the blade for possible post-test examination. One of the anomalous areas over the spar, between stations 36 and 48 in Figure 19b, was selected for observation during the test.

---

* Note: shearography is much less susceptible to environmental noise than other coherent inspection techniques, but a few millimeters of motion is enough to foil it. The rope referred to was quite sufficient for shearography, but ESPI or holometry would have been impossible under these conditions.

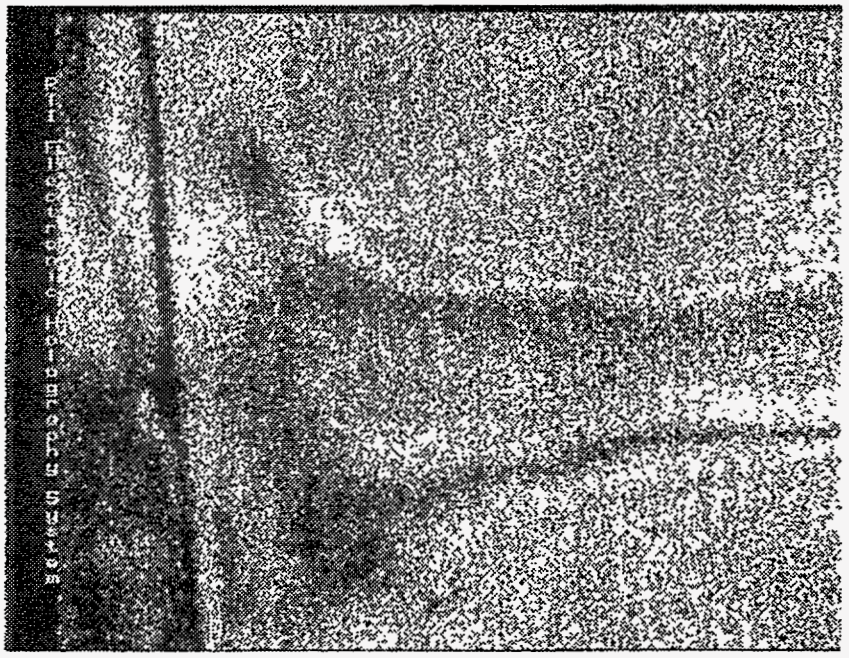

Figure 36. Pre-test shearogram using thermal stress, station 240 to 252.

The 36 to 48 station view was also inspected while being stressed by tension and compression, to compare with thermal stressing. These stresses were applied by forcing the blade tip to the side by hanging weights (about ten pounds) on the tip rope visible in Figure 34. All three stress methods show the main blade spar (longitudinal) and some structure associated with the angled leading edge in that area. The thermal stress showed more detailed deformations, which could be either skin delaminations or thickness variations. None of these tests had strong flaw indications.

4.3.2 Real-Time Test Results

During the blade test, an area near the root was selected for continuous monitoring with the shearography system. This area had shown an anomaly that was assumed to be a debond or delamination. While there was not enough information to predict where the blade would fail, this anomalous area was judged likely to show changes during blade stressing. It was also necessary to select an area near the root, to avoid problems with the gross motion (several feet) of

the outer portions of the blade. The optical head was supported above the root area as shown in Figure 35 during the failure test, and the results were monitored from within the control room.

During the test, the optical head was arranged to look down on the area between stations 36 and 48, as shown in Figure 35. While the blade was being subjected to the large forces and deflections necessary to stress it to failure, skin deformations rapidly exceeded the measurement range of shearography. However, the leakage in the hydraulic system at each step in the loading sequence see (Figure 6a) provided a convenient delta-load for shearographic measurements. A change of about 10 pounds gave a reasonable number of fringes. Although some change in character of the deformation was observed, no obvious flaws or breakage appeared. Figure 37 shows typical results at two different base loads in this area.

4.3.3 Post-Test Results

The area between stations 36 to 48 was inspected after the test, again using thermal stress. Figure 38 shows shearograms of this area, before and after the blade test. It appeared that the anomaly grew during the test. The post-mortem of this area showed a debonding of the spar and the skin (also discussed above). The original indication of a suspected "problem" in this area can be attributed to a thinning of blade skin. Shearography indicated that the deformation of this section was significantly different from its surroundings. The post-mortem was required to determine that the difference was attributable to a thin skin.

Several small flaws were noted and marked on the blade skin during the pre-test examination. Two flaws, near the transition from the circular root to an airfoil blade section, had significant AE activity during the blade loading. Post-test shearographic inspection of this area using thermal stress revealed that the two flaws had grown in size. Both flaws appeared to be small [approximately 1.4 in. (3.5 cm) in diameter], near-surface delaminations, and probably were not structurally significant. A shearogram of one of these flaws is shown in Figure 39. A post-mortem examination of one of the flaws showed that it was a region of high porosity (a manufacturing "bubble") near the surface of the blade. Under microscopic examination, the flaw showed evidence that it had grown (approximately doubling in size) during the course of the experiment.

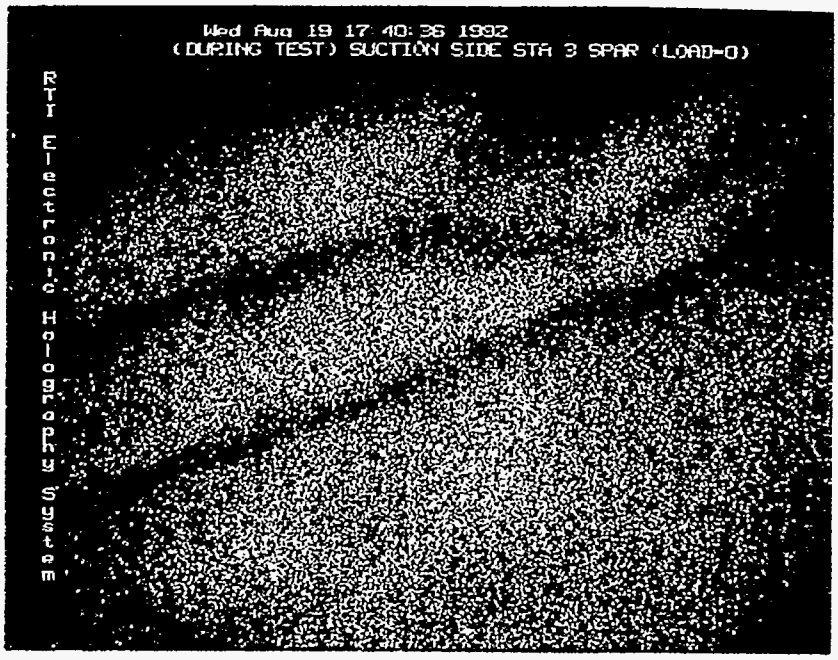

Figure 37a. 0 to 10 pounds load.

Figure 37b. 6364 to 6375 pounds load.

Figure 37. Real-time shearograms using differential loads, station 36 to 48.

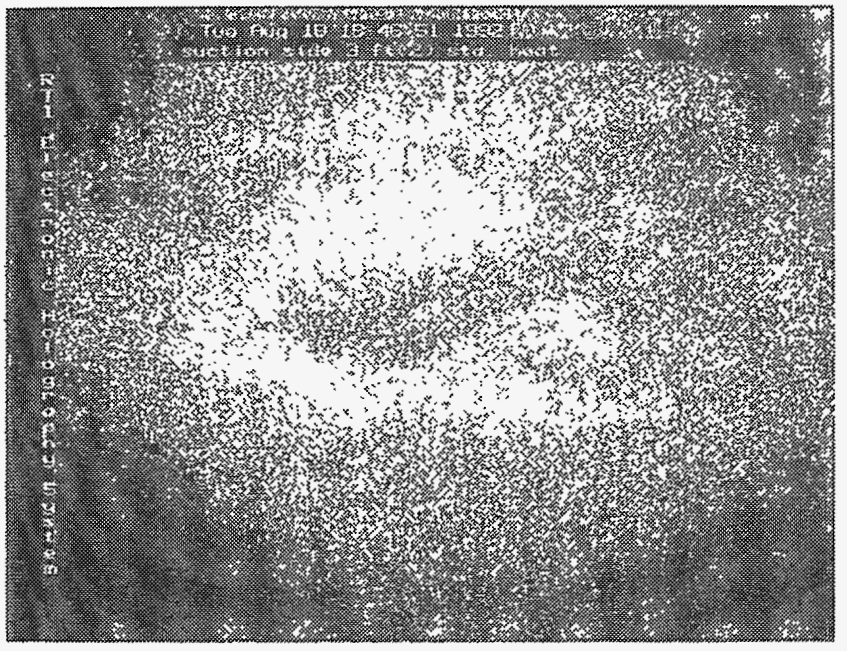

Figure 38a. Before the failure test.

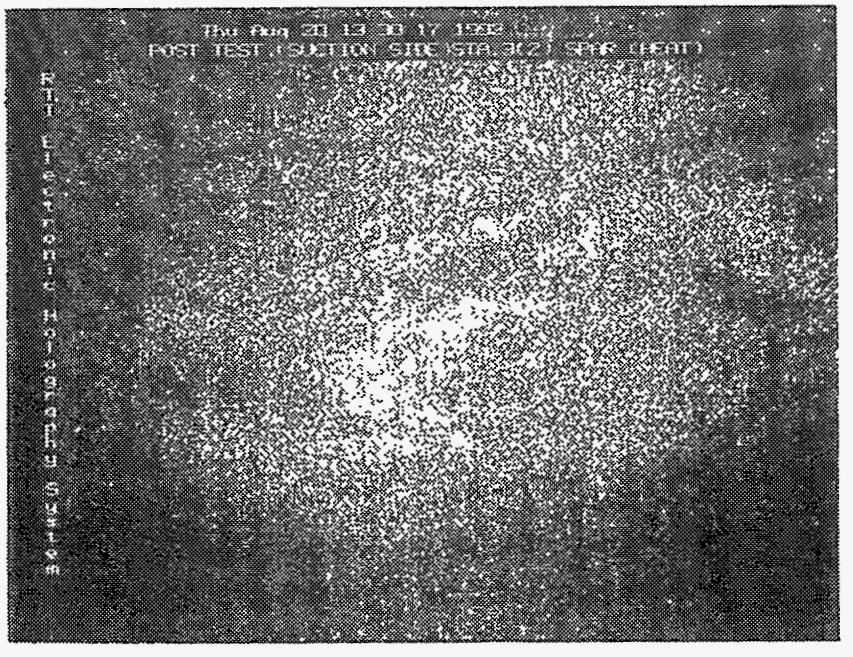

Figure 38b. After the failure test.

Figure 38. Shearograms using thermal stress, station 36 to 48.

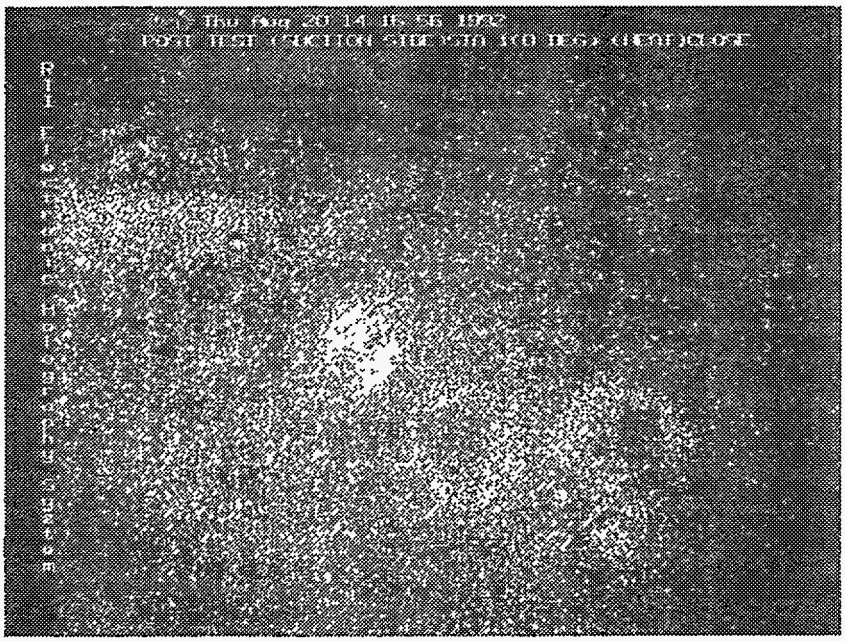

Figure 39. Shearogram of the flaw at station 24. The two circles with dark centers are where acoustic emission sensors 13 and 9 were located—the remaining adhesive caused these indentions. The bright circle above and left of the transducer locations is the flaw.

After the blade failed, there was clearly a delamination between the spar and the skin in the area of failure. This area was examined with shearography, again using thermal stress, to determine how well shearography could locate the end of the debonded area. The shearographic image indicated a discontinuity starting at about station 224.

Another discontinuity was indicated near station 124. Figure 40 is a shearogram from station 120 to 132. A discontinuity is indicated at about station 124. Post-test inspections showed that the spar had debonded from the skin in the area.

4.4 Discussion

As mentioned in Section 4.1, coherent optical techniques are sensitive to surface motion, and hence to environmental factors such as acoustic vibrations or temperature variations. In this test, shearography was used since it is more robust against these disturbances than is ESPI. However, natural blade vibrations when the blade was held only at the root made even

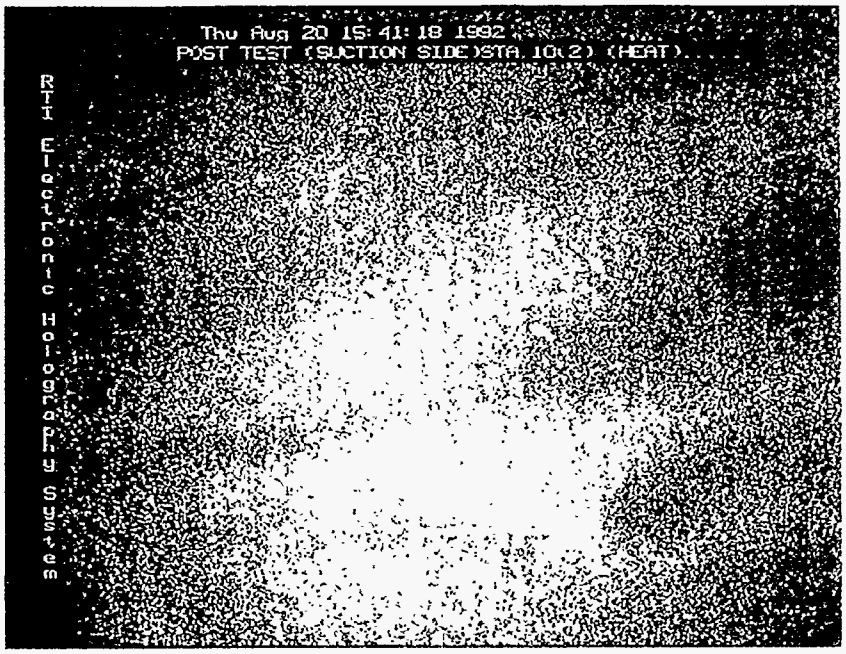

Figure 40. Post-test shearogram of the spar/skin bond failure, station 120 to 132. The dark areas at Station 124 are the end of the bonded area.

shearography impossible except near the root. This was easily solved by constraining the tip with a rope.

For the pre-test inspection, partial coverage of one side of the blade and the root (55 views total) took almost two days, including equipment setup. The testing was slowed by equipment problems -- the laser was unstable and quite a bit of time was spent waiting for it to settle. Without this problem, the area tested could perhaps have been covered in a single day. In any case, significant time was spent moving equipment, re-positioning the associated test hardware to allow a clear view, etc. The relatively long cable (50 feet) between the optical head and the electronics rack was a definite advantage -- the rack was only moved a few times. During the static test itself, the coherent optical inspection followed the test in real time, and little if any delay was added for data taking. However, only one small portion of the blade could be monitored.

Despite the problems discussed here, the shearography technique was able to locate manufacturing flaws (areas of high porosity), relatively thin skin sections, structural supports (as with the spar) and structural discontinuities (at the end of the spar).

5. CONCLUDING REMARKS

The results given here strongly support the use of acoustic emission in both evaluating blade design and in proof testing blades after their manufacture. This technique followed the initial failure of the blade in real time and was able to locate other areas where damage was accumulating. Additional tests on this blade verified these active AE areas as potential failure zones. Although the coherent optical test results were highly encouraging, the use of this technique is currently best limited to QA procedures rather than to field inspections. In a dedicated installation, with proper handling equipment and fixturing for the blade, many of the aforementioned environmental stability problems can be solved. Also, with proper handling and mounting for the optical equipment, it would be possible to do a complete surface inspection in a few hours. This technique has been demonstrated in a production environment in the aerospace industry.

6. REFERENCES

1. Bertelsen, W.D., and M.D. Zuteck. 1990. *Investigation of Fatigue Failure Initiation and Propagation in Wind-Turbine-Grade Wood/Epoxy Laminate Containing Several Veneer Joint Styles.* DOE/SBIR DE-AC02-86ER80385 Phase 2 Report. Gougeon Brothers.

2. Beattie, A.G. 1983. "Acoustic Emission, Principles and Instrumentation." *J. of Acoustic Emission.* Vol. 2, Number 1/2, p. 95.

3. Vest, C.M. 1979. *Holographic Interferometry.* John Wiley & Sons, New York.

4. Musial, W., and J. Allread. 1993. " Test Methodology and Control of Full-Scale Fatigue Tests on Wind Turbine Blades." *Wind Energy-1993*, SED-Vol. 14, American Society of Mechanical Engineers, New York, pp. 199-206.

5. Tangler, J.L., and D.M. Somers. 1987. " Status of the Special-Purpose Airfoil Families." *Proceedings of Windpower '87. San Francisco, CA.* SERI/TP-3264. National Technical Information Service, Springfield, VA.

6. Tangler J., B. Smith, D. Jager, E. McKenna, and J. Allread. 1989. "Atmospheric Performance Testing of the Special-Purpose SERI Thin Airfoil Family: Preliminary Results." *Proceedings of Windpower '89.* San Francisco, CA.

DISTRIBUTION:

R. E. Akins
Washington & Lee University
P.O. Box 735
Lexington, VA 24450

M. Anderson
Renewable Energy Systems, Ltd.
Eaton Court, Maylands Avenue
Hemel Hempstead
Herts HP2 7DR
ENGLAND

H. Ashley
Dept. of Aeronautics and
Astronautics Mechanical Engr.
Stanford University
Stanford, CA 94305

P. Bach
ECN Energy Engineering
P.O. Box 1
1755 ZG Petten
the Netherlands

C. P. Butterfield
NREL
1617 Cole Boulevard
Golden, CO 80401

G. Bywaters
Northern Power Systems
Box 659
Moretown ,VT 05660

R. N. Clark
USDA
Agricultural Research Service
Southwest Great Plains Research Center
Bushland, TX 79012

C. Coleman
Northern Power Systems
Box 659
Moretown, VT 05660

J. C. M. de Bruijn
KEMA-KIM/KR
P.O. Box 9035
6800 ET Arnhem
the Netherlands

O. Dyes
Wind/Hydro/Ocean Div.
U.S. Department of Energy
1000 Independence Avenue, SW
Washington, DC 20585

A. J. Eggers, Jr.
RANN, Inc.
260 Sheridan Ave., Suite 414
Palo Alto, CA 94306

D. M. Eggleston
DME Engineering
P.O. Box 5907
Midland, TX 79704-5907

P. R. Goldman
Wind/Hydro/Ocean Division
U.S. Department of Energy
1000 Independence Avenue
Washington, DC 20585

I. J. Graham
Dept. of Mechanical Engineering
Southern University
P.O. Box 9445
Baton Rouge, LA 70813-9445

G. Gregorek
Aeronautical & Astronautical
Dept.
Ohio State University
2300 West Case Road
Columbus, OH 43220

C. Hansen
University of Utah
Department of Mechanical Engineering
Salt Lake City, UT 84112

R. Heffernan
Kenetech Windpower, Inc.
6952 Preston Avenue
Livermore, CA 94550

L. Helling
Librarian
National Atomic Museum
Albuquerque, NM 87185

W. E. Holley
Kenetech Windpower
6952 Preston Avenue
Livermore, CA 94550

S. Hock
Wind Energy Program
NREL
1617 Cole Boulevard
Boulder, CO 80401

M. A. Ilyan
Pacific Gas and Electric Co.
3400 Crow Canyon Road
San Ramon, CA 94583

B. J. Im
McGillim Research
4903 Wagonwheel Way
El Sobrante, CA 94803

K. Jackson
Dynamic Design
123 C Street
Davis, CA 95616

L. Jea
Loral Vought Systems
Mail Stop SP79
P.O. Box 650003
Dallas, TX 75265-0003

O. Krauss
Division of Engineering Research
Michigan State University
East Lansing, MI 48825

C. Lange
Civil Engineering Dept.
Stanford University
Stanford, CA 94305

A. Liniecki
Mechanical Engineering Department
San Jose State University
One Washington Square
San Jose, CA 95192-0087

G. A. Lowe
Univ. of the West of England
Bristol, Faculty of Engineering
Coldharbour Lane Frenchay
Bristol, UK

R. Lynette
R. Lynette & Assoc., Inc.
15042 NE 40th Street
Sutie 206
Redmond, WA 98052

P. H. Madsen
Riso National Laboratory
Postbox 49
DK-4000 Roskilde
DENMARK

D. Malcolm
R. Lynette & Associates, Inc.
15042 N.E. 40th Street, Suite 206
Redmond, WA 98052

J. F. Mandell
Montana State University
302 Cableigh Hall
Bozeman, MT 59717

A. Mikhail
Zond Systems, Inc.
13000 Jameson Road
P.O. Box 1910
Tehachapi, CA 93561

S. Miller
162636 NE 19th Place
Bellevue, WA 98008-2552

R. H. Monroe
Gougeon Brothers
100 Patterson Avenue
Bay City, MI 48706

D. Morrison
New Mexico Engineering
Research Institute
Campus P.O. Box 25
Albuquerque, NM 87131

W. Musial (25)
Wind Energy Program
NREL
Boulder, CO 80401

V. Nelson
Department of Physics
West Texas State University
P.O. Box 248
Canyon, TX 79016

G. Nix
NREL
1617 Cole Boulevard
Golden, CO 80401

J. W. Oler
Mechanical Engineering Dept.
Texas Tech University
P.O. Box 4289
Lubbock, TX 79409

R. Osgood
NREL
1617 Cole Boulevard
Golden, CO 80401

C. Paquette
The American Wind Energy Association
777 N. Capitol Street, NE
Suite 805
Washington, DC 20002

B. Maribo Pedersen
Techn. University Denmark
Bld. 404, Lundtoftevej 100
DK-2800
Lynby, Denmark

R. G. Rajagopalan
Aerospace Engineering Department
Iowa State University
404 Town Engineering Bldg.
Ames, IA 50011

R. Rangi
Manager, Wind Technology
Dept. of Energy, Mines and Resources
580 Booth 7th Floor
Ottawa, Ontario K1A 0E4
CANADA

M. G. Real, President
Alpha Real Ag
Feldeggstrasse 89
CH 8008 Zurich
SWITZERLAND

R. L. Scheffler
Research and Development Dept.
Room 497
Southern California Edison
P.O. Box 800
Rosemead, CA 91770

L. Schienbein
Battelle-Pacific Northwest Laboratory
P.O. Box 999
Richland, WA 99352

T. Schweizer
Princeton Economic Research, Inc.
12300 Twinbrook Parkway
Suite 650
Rockville, MD 20852

J. Sladky, Jr.
Kinetics Group, Inc.
P.O. Box 1071
Mercer Island, WA 98040

M. Snyder
Aero Engineering Department
Wichita State University
Wichita, KS 67208

K. Starcher
AEI
West Texas State University
P.O. Box 248
Canyon, TX 79016

F. S. Stoddard
Second Wind, Inc.
7 Davis Square
Somerville, MA 02144

D. Taylor
Alternative Energy Group
Walton Hall
Open University
Milton Keynes MK7 6AA
UNITED KINGDOM

G. P. Tennyson
DOE/AL/ETD
Albuquerque, NM 87115

W. V. Thompson
410 Ericwood Court
Manteca, CA 95336

R. W. Thresher
NREL
1617 Cole Boulevard
Golden, CO 80401

W. A. Vachon
W. A. Vachon & Associates
P.O. Box 149
Manchester, MA 01944

B. Vick
USDA
Agricultural Research Service
Southwest Great Plains Research Center
Bushland, TX 79012

V. Wallace
FloWind Corporation
990 A Street, Suite 300
San Rafael, CA 94901

L. Wendell
Battelle-Pacific Northwest
Laboratory
P.O. Box 999
Richland, WA 99352

R. E. Wilson
Mechanical Engineering Dept.
Oregon State University
Corvallis, OR 97331

S. Winterstein
Civil Engineering Department
Stanford University
Stanford, CA 94305

R. Yetka
EM&A Department
2348 Engineering Hall
1415 Johnson Drive
Madison, WI 53706-1691

M. Zuteck
MDZ Consulting
931 Grove Street
Kemah, TX 77565

MS 0100	Document Processing, Org. 7613-2 (10) For DOE/OSTI
MS 0129	J. C. Clausen, Org. 12620
MS 0437	E. D. Reedy, Org. 1562
MS 0439	C. Dohrmann, Org. 1434
MS 0439	D. W. Lobitz, Org. 1434
MS 0439	D. R. Martinez, Org. 1434
MS 0443	J. G. Arguello, Org. 1561
MS 0557	T. G. Carne, Org. 2741
MS 0557	G. H. James III, Org. 2741
MS 0615	A. Beattie, Org. 2752
MS 0615	B. Hansche, Org. 2752
MS 0615	W. Shurtleff, Org. 2752
MS 0619	Technical Publications, Org. 151
MS 0708	H. M. Dodd , Org. 6214 (50)
MS 0708	T. D. Ashwill, Org. 6214
MS 0708	D. E. Berg, Org. 6214
MS 0708	D. P. Burwinkle, Org. 6214 (NMERI)
MS 0708	M. A. Rumsey, Org. 6214
MS 0708	L. L. Schluter, Org. 6214
MS 0708	H. J. Sutherland, Org. 6214
MS 0708	P. S. Veers, Org. 6214
MS 0899	Technical Library, Org. 7141 (5)
MS 9018	Central Technical Files, Org. 8523-CTF